ERDC TR-21-10

Engineer Research and Development Center

US Army Corps of Engineers®
Engineer Research and Development Center

ERDC
ENGINEER RESEARCH & DEVELOPMENT CENTER

Remote Assessment of Infrastructure for Ensured Maneuver (RAFTER)

Multi-Objective Source Scaling Experiment

R. Daniel Costley, Luis A. De Jesús Díaz, Sarah McComas,
Christopher P. Simpson, James W. Johnson,
and Mihan H. McKenna

June 2021

Multi-Objective Source Scaling Experiment

R. Daniel Costley, Luis A. De Jesús Díaz, Sarah McComas, Christopher P. Simpson, and Mihan H. McKenna

Geotechnical and Structures Laboratory
U.S. Army Engineer Research and Development Center
3909 Halls Ferry Road
Vicksburg, MS 39180

James W. Johnson

Information Technology Laboratory
U.S. Army Engineer Research and Development Center
3909 Halls Ferry Road
Vicksburg, MS 39180

Final report

Approved for public release; distribution is unlimited.

Prepared for U.S. Army Corps of Engineers
Washington, DC 20314-1000

Under Project 62784/T40/24 and 622146/AR9/02,"Remote Assessment of Critical Infrastructure" (RACI) and "Remote Assessment of Infrastructure for Ensured Maneuver" (RAFTER)

Abstract

The U.S. Army Engineer Research and Development Center (ERDC) performed an experiment at a site near Vicksburg, MS, during May 2014. Explosive charges were detonated, and the shock and acoustic waves were detected with pressure and infrasound sensors stationed at various distances from the source, i.e., from 3 m to 14.5 km. One objective of the experiment was to investigate the evolution of the shock wave produced by the explosion to the acoustic wavefront detected several kilometers from the detonation site. Another objective was to compare the effectiveness of different wind filter strategies. Toward this end, several sensors were deployed near each other, approximately 8 km from the site of the explosion. These sensors used different types of wind filters, including the different lengths of porous hoses, a bag of rocks, a foam pillow, and no filter. In addition, seismic and acoustic waves produced by the explosions were recorded with seismometers located at various distances from the source. The suitability of these sensors for measuring low-frequency acoustic waves was investigated.

Contents

Abstract ii

Figures and Tables iv

Preface vii

1 Introduction 1

2 Experiment Setup and Instrumentation: 4

2.1 Source description 4
2.2 Weather 5
2.3 Instrumentation 8
2.3.1 Near-field *8*
2.3.2 Mid-field *10*
2.3.3 Far-field infrasound sensors *11*
2.3.4 Instrumentation site *12*
2.3.5 Microphones and geophones *15*

3 Analysis and Results 18

3.1 Shock wave 18
3.2 Propagation 19
3.3 Time of arrival 23
3.4 Wind filter analysis 26
3.5 Acoustic seismic coupling 31

4 Summary 48

References 50

Appendix A: Photograph of the Sensors Deployed at Instrumentation Site 52

Appendix B: Time Series Recorded at Instrumentation Site 53

Appendix C: Background Noise Recorded at Instrumentation Site 55

Appendix D: SNR Recorded at Instrumentation Site 57

Appendix E: Seismometer Response to Acoustic Waves Produced by Airblast 59

Unit Conversion Factors 61

Report Documentation Page

Figures and Tables

Figures

Figure 1. Overview map of the Big Black Test Site with the shot location (red star) for the test series. 5

Figure 2. Upper plot: Sound speed profile at the initial shot (11:48:43 CDT, green) and after last shot (14:13:35 CDT, blue). Middle: Wind direction at the initial shot (11:48:43 CDT, red) and after last shot (14:13:35 CDT, blue). Lower: Wind direction at the initial shot (11:48:43 CDT, red) and after last shot (14:13:35 CDT, blue). 7

Figure 3. Radial layouts of pressure transducers (East, North, West Southwest). The red circle illustrates the shot location while the black circles represent the pressure transducer locations. 9

Figure 4. Pressure transducer mount (left) and installed mount (right). 10

Figure 5. Overview map showing the location of the three of the Validyne sensors, B030, B060, and B125, with relation to the shot location. 10

Figure 6. Overview map showing locations of far-field instrumentation (Table 5) in relation to the shot location. The red circles represent 5, 10, and 15 km from the shot location. 13

Figure 7. Example of an IML sensor with four porous hoses. 14

Figure 8. Top: Locations of Validynes, geophones, and microphones to distances of 2km from source; middle: Zoomed-in view of the geophone and microphone arrays at 0.5 km from source; bottom: Zoomed-in view of the microphone and geophones at the Instrumentation site, approximately 8.44 km from the source. 16

Figure 9. Shock waves from shots 1 and 4 recorded with the Kulite pressure transducers. Top left – shot 1 at 3.05 m; top right – shot 1 at 12.19 m; bottom left – shot 4 at 3.05 m; bottom right – shot 4 at 12.19 m. 19

Figure 10. BlastX predictions plotted alongside measured peak pressure as a function of distance from the source. The top plot is for shot 1; bottom plot is for shot 4. 20

Figure 11. Time series associated with shot 4 for all sensors in the Step Out Array. 21

Figure 12. Peak amplitude as a function of source-receiver spacing. 22

Figure 13. Peak amplitude, in decibels, versus scaled distance. 22

Figure 14. TOA versus range for all sensors at shot 4. 23

Figure 15. Time of arrival (TOA) versus range for the near-field sensors for shot 5 (top) and shot 4 (bottom). 25

Figure 16. TOA versus range for the far-field sensors from all shots. 25

Figure 17. Top: Signals recorded from shot 2 with the Chaparral sensors. Bottom: Signals recorded from shot 2 with the IML and Hyperion sensors. The numbers in the legends correspond to the Sensor numbers in Table 6. 27

Figure 18. Top: Signals recorded from shot 2 with the Chaparral sensors. Bottom: Signals recorded from shot 2 with the IML and Hyperion sensors. The numbers in the legends correspond to the Sensor numbers in Table 6. 28

Figure 19. Background noise recorded with the Chaparral, IML, and Hyperion sensors listed in Table 6. Top: Background noise before the first shot. Bottom: Background noise after last shot. 29

Figure 20. Top left: SNR calculated from shot 2 with the Chaparral sensors. Top right: SNR calculated from shot 2 with IMLs and Hyperions. Bottom left: SNR calculated from shot 4 with Chaparral sensors. Bottom right: SNR calculated with the IML and Hyperion sensors from shot 4. Numbers in the legends correspond to the Sensor numbers in Table 6. 30

Figure 21. Top: Time series waveforms of seismic arrivals for sensors at 30, 60, and 125 m. The time series is cut off at the time just before arrival of the air shock, which overwhelms the vertical scale; middle: Times of arrival for all 5 tests corresponding to these same sensors; bottom: Peak amplitudes for all 5 shots. 33

Figure 22. Time series waveforms of shock arrivals for shot 3, recorded by geophones ranging from 7 m to 8440 m from source. 35

Figure 23. Top: Time of arrival of shock wave as recorded with geophones. The line represents a least-squares fit to the data. Bottom: Magnitude of negative peak of shock wave as recorded with geophones. 36

Figure 24. The acoustic arrival recorded from shot 3 with geophones and microphones located at the ranges indicated. 37

Figure 25. The transfer and coherence functions between acoustic signals from the explosion recorded with microphones and geophones at three distance from the source: top – 516 m; middle – 2,070 m; bottom – 8,434 m. The red dots on the curves indicate points for which the coherence is greater than 0.9. The numbers in the legend at top indicate the shot number. 39

Figure 26. Schematic showing geometry used to determine DOA. The green ‘x’ symbols represent the sensors. The blue line that intersects the sensor on the right represents a plane wave. The red dashed curve represents a spherical wave front originating from the source, exaggerated in drawing. Detailed explanation is provided in text. 41

Figure 27. The horizontal components plotted with respect to time for the 3C geophones located at 8,440 m and 8,434 m from the source. 43

Figure 28. The horizontal components plotted for different time segments for the 3C geophones located at 8,440 m (top) and 8,434 m (bottom) from the source. In each plot, the black line is parallel to the back azimuth from the receiver to the source, calculated from GPS data. 45

Tables

Table 1. Test matrix for series shots for MOSSE. 5

Table 2. XT-190 specifications and setup. 9

Table 3. The distance of the Validyne sensors used for the mid-field range. 11

Table 4. The Validyne sensor specification. 11

Table 5. The IML sensors used for the far-field range. 12

Table 6. Sensors used in the Instrumentation site wind filter study. 14

Table 7. Geophones and microphones from near-field to instrumentation array. 17

Table 8. Back azimuths measured with 3-microphone array shown in Figure 8 for all 5 shots. N-S, W-S, and N-W correspond to the 3 pairs of microphones at the vertices. The error is the difference between the measured azimuth and that determined from ground truth, 145.7°. 42

Table 9. Back azimuths measured with 3C seismometer and geophone for all 5 shots. The error is the difference between the measured azimuth and that determined from ground truth, 145.7°. 47

Preface

This study was prepared for the U.S. Army Corps of Engineers and conducted for the Office of the Assistant Secretary of the Army for Acquisition, Logistics, and Technology (ASAALT) under Project "Remote Assessment of Critical Infrastructure" (RACI) and task "Remote Assessment of Infrastructure for Ensured Maneuver" (RAFTER) under the Persistent Geophysical Sensing – Infrasound (PGSI) project. The technical monitor was Military Engineering.

The work was performed by the Structural Engineering Branch (GSS) of the Geosciences and Stuctures Division (CS) of the Geotechnical and Structures Laboratory (ERDC-GSL) and the Sensor Integration Branch (SIB) of the Computational Science and Engineering Division (CSED) of the Information Technical Laboratory (ITL). Both GSL and ITL are part of the U.S. Army Engineer Research and Development Center. At the time of publication, Ms. Mariely Mejias-Santiago was Chief, GSS; Mr. James L. Davis was Chief, GS; Mr. Quincy Alexander was Chief, SIB; Dr. Jerry Ballard was Chief, CSEB. Ms. Pamela G. Kinnebrew, GZT, was the Technical Director for Military Engineering. The Deputy Director of ERDC-GSL was Mr. Charles W. Ertle II, and the Director was Mr. Bartley P. Durst. The Deputy Director of ERDC-ITL was Ms. Patti Duett, and the Director was Dr. David Horner.

COL Teresa A. Schlosser was the Commander of ERDC, and Dr. David W. Pittman was the Director.

The authors thank Dr. Chris Hayward of Southern Methodist University for the assistance with designing and executing MOSSE; Mr. Kenneth McLaughlin and Mr. Jesse Howard for wonderful support fielding the instrumentation for the experiment; Mr. Brian Quinn (currently at Cold Regions Research Engineering Laboratory) for launching radisondes balloons and recording meteorological data; Mr. Alex Baylot and Ms. Linda Jackson for providing property for the step out and instrumentation arrays; and Mr. Charles W. Ertle and Mr. Kevin Tillman for coordinating the test site and explosive charges.

1 Introduction

Shock-wave propagation from explosions transition from being strongly non-linear in the near field, to weakly non-linear in the transition region (midfield), to linear sound propagation in the farfield (Whitaker and Norris 2008). The transition to the linear regime is associated with a decay in amplitude. Many factors contribute to this behavior. Geometrical spreading, molecular absorption, turbulence, and scattering are some of the mechanisms involved. Also, wind and temperature gradients in the atmosphere cause refraction, which can either increase or decrease sound pressure levels significantly (Embleton 1996). There are many other variables that affect the propagation of acoustic waves outdoors. There have been numerous observations and studies of the relationship of peak pressures to range and charge weight and almost all of them have concentrated on the peak pressure value, the observed impulse, or characteristic pulse times of the initial shock (Kinney and Graham 1985). This study will focus on characterization of the transition of the wavefront from shock to linear acoustic propagation utilizing a set of well-defined controlled sources.

Another area of interest for the recording of acoustic and infrasonic signals is the effect wind filters cause on impulsive signals. Although they can improve the signal-to-noise ratio, especially in windy conditions, they can also attenuate and phase shift the signal. Historically the infrasound community has used micro-porous hoses (soaker hoses) as wind filters for their microphones, which sum the coherent acoustic energy over the area sampled by the hoses (Howard et al. 2007; Noel and Whitaker 1991; Walker and Hedlin 2010). Previous researchers have used from 1 to 12 hoses with lengths from a meter or less to 30 m in linear or star arrangements. When the hoses are intact and deployed correctly, they do appear to reduce the noise from 1 to 3 m/s winds, but one of the drawbacks of these filters is environment deteriation, e.g., debris filling pores or breakdown hose material creating holes, which reduces their effectiveness (Haak and De Wilde 1996). Therefore, this experimental series aims to investigate alternative wind-noise mitigation strategies that would be readily available and not suffer from the same environmental degradation as the hoses.

Furthermore, while there have been indirect laboratory tests of the effectiveness of various hose brands (formulations) on signal propagation characteristics, there have not been calibrated demonstrations of using broadband acoustic signals in the field. While there have been indirect measurements of the spectral magnitude effect of hoses (Kim et al. 2004), there have not been controlled measurements to demonstrate the effect of hoses on high-frequency impulsive signals where the effect should be most pronounced.

Another area of interest is acoustic-seismic coupling. Albert et al. (2013) performed studies on ground vibrations produced by near-surface explosions. This work compared the ground vibrations of different types of surfaces, including hard and soft soils and snow. They recorded the propagating acoustic waves with microphones. Geophones detected and recorded direct seismic arrivals as well as the ground vibration associated with the blast and acoustic wave.

This report describes tests performed on 21 May 2014 in which different size explosive charges were detonated at the same height above ground. Pressure sensors, infrasound sensors, broadband acoustic microphones, and seismometers had been deployed at distances from the source ranging from 3 m to 13 km. The airborne shock and acoustic waves produced by the explosions were analyzed in three regimes, referred to as near-field, mid-field, and far-field. In the near-field, pressure transducers recorded the passage of the airborne shock wave. The shock transformed into a non-linear acoustic wave in the mid-field, which was recorded by a different type of pressure transducer. The amplitude of the acoustic waves in this regime exceeded the dynamic range of several of these sensors and, as a result, many of these measurements were clipped, especially at the closer ranges and with the larger explosions, discussed in more detail in Chapter 3. Infrasound sensors and broadband microphones were deployed at the greater source-to-receiver distances that made up the far-field. The acoustic waves produced by the explosion in the far-field could generally be described by linear acoustic models.

At a site 8.4 km from the point of the explosions, sensors were deployed using a variety of wind-filtering strategies. The types of wind filters are evaluated by comparing the signals and background noise recorded with them.

In addition to the sensors mentioned, geophones were deployed at ranges varying from 7 m to 8.4 km. The explosions created seismic waves that were detected out to distances of 125 m. The geophone response to the airborne shock wave, i.e., the acoustically coupled seismic wave, was also investigated. The wave speeds of the airborne shock waves and acoustic waves measured with geophones compared favorably with those determined from the infrasound sensors. An effort was made to quantify the response between closely spaced vertical geophones and broadband microphones in order to determine the fidelity with which the geophones measure the airborne waves. Finally, the signals recorded with arrays of geophones and microphones were processed in an effort to determine direction of arrival (DOA). In addition, the signals recorded with horizontal components of 3-component (3C) seismometers were processed as vector sensors to determine DOA. The two approaches were compared.

The following chapter describes the experiment and the configuration of the deployed sensors. Chapter 3 presents the signal processing approaches used to analyze the data. Results are also presented. Finally, Chapter 4 provides a brief summary and conclusions for this work.

2 Experiment Setup and Instrumentation

The experiment was completed at the Big Black Test Site (BBTS), a U.S. Army Engineer Research and Development Center (ERDC) facility. The facility is capable of supporting explosive charges up to 24 lb. A total of five shots were conducted in the same source location and ground height starting from smallest to largest and then with a repeat of the smallest shot at the end of the sequence. The test matrix is outlined in Table 1 . The shots were completed within 1 hr to limit the change in propagation characteristics. Details of the source, propagation characteristics, and instrumentation used in the experiment will be explained in the following subsections.

2.1 Source description

The sources for this experiment were spherical charges of Composition C4 plastic explosives, which upon detonation created a pressure front. These shots detonated at the BBTS, which is capable of supporting explosive charges up to 24 lb during the summer test season. Table 1 displays the test series completed to achieve the aim of the experiment and explained in the above section. Figure 1 provides an overview of the BBTS facility with the shot location labeled.

Five spherical charges were detonated at the same source location with a height above ground of 1.22 m (4 ft), starting from the smallest to largest weight, with a repeat of the smallest shot at the end of the sequence. Shots were completed midday central daylight time (CDT) and within a single hour to reduce the variability in propagation characteristics. To determine the precise times for the detonations listed in Table 1, a conducting wire was placed on each charge. The wire break, which indicated the precise time of the detonation, was recorded with a Reftek 125A digitizer. In plots showing pressure waveforms, time t = 0 sec corresponds to the wire break time.

Figure 1. Overview map of the Big Black Test Site with the shot location (red star) for the test series.

Table 1. Test matrix for series shots for MOSSE.

Shot No.	Size (kg)	Size (lb)	TNT Equivalent (lb)	UTC	CDT
1	0.57	1.25	1.675	16:40:33.144	11:40:33.144
2	1.36	3	4.02	16:57:07.285	11:57:07.285
3	4.54	10	13.4	17:11:13.432	12:11:13.432
4	10.91	24	32.16	17:26:35.559	12:26:35.559
5	0.57	1.25	1.675	17:40:35.011	12:40:35.011

2.2 Weather

Radiosonde balloons were launched at 11:48 and 14:14 local time (CDT). The first balloon was launched 8 min after the first shot, and the second balloon was launched 1 hr and 34 min after the last shot. The radiosondes collected temperature, wind speed, and wind direction data at altitudes between 0.05 km and 25 km. The temperature profiles from each radiosonde launch were used to calculate the adiabatic sound speed (c, m/s) following Equation 1 where T is the temperature in Kelvin (Pierce 1989).

$$c = 331 + 0.6T \tag{1}$$

The sound speed profile decreases as the altitude increases, up to 14.5 km. This profile, common for sunny days this time of year, causes the sound to refract upward over the ranges of interest in this experiment, which was 14.5 km. Realistically, at propagation distances for this experiment, the meteorological conditions at altitudes greater than 2 km have a minimal effect on acoustic propagation; therefore, analysis of metrological conditions will focus on the lower 2 km.

Figure 2 shows the profiles for the adiabatic speed of sound, wind speed, and wind direction for altitudes up to 2 km. During the experiment, the sound speed changed approximately 2 m/s for altitudes less than 1 km (Figure 2).

The radiosondes did not record temperature until they reached an altitude of 50 m. The data collected from the Jackson-Medgar Wiley Evers International Airport were used to estimate the meteorological conditions at ground level, which is approximately 80 km to the east of the test site. The ground conditions were relatively stable during the time of the test, the temperature varied from 28.3°C to 29.0°C, the wind speed was between 2.6 to 4.1 m/s, and the wind direction was S to SSW. The plots show that the wind speed near the ground increased during test time and increased for altitudes above 300 m.

Figure 2. Upper plot: Sound speed profile at the initial shot (11:48:43 CDT, green) and after last shot (14:13:35 CDT, blue). Middle: Wind direction at the initial shot (11:48:43 CDT, red) and after last shot (14:13:35 CDT, blue). Lower: Wind direction at the initial shot (11:48:43 CDT, red) and after last shot (14:13:35 CDT, blue).

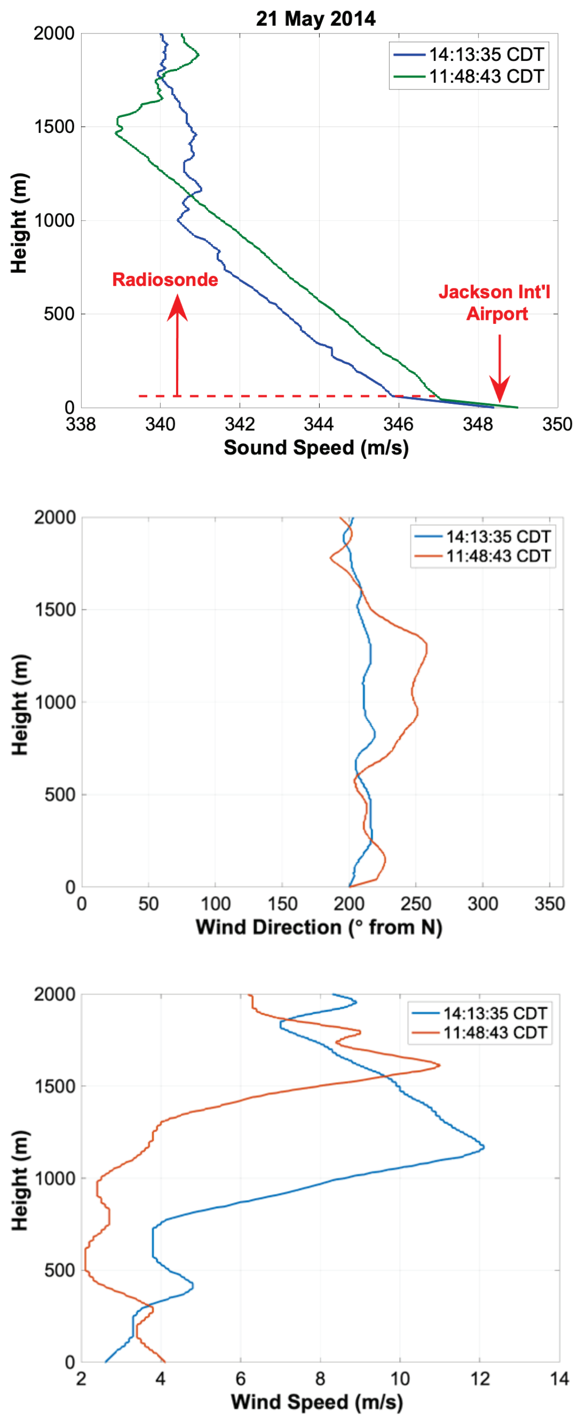

2.3 Instrumentation

In order to understand the transition of the pressure field from shock to linear propagation, sensors were deployed in groups at different ranges. These groups are denoted near-field (Kulite), mid-field (Validynes), and far-field (Inter-Mountain Labs infrasound sensor [IML]). Sensors located in the near- and mid-field range were used to investigate the transition region between shock propagation and linear acoustics; however, at mid-field ranges, the pressures were often above the dynamic range of the sensors and, as a result, the recorded signals clipped.

2.3.1 Near-field

Pressure transducers positioned along radials East, North, and West Northwest from the source location were used to instrument the near-field site. Each radial contained four pressure transducers at ranges of 3.048, 6.096, 12.19, and 24.38 m (shown as 10, 20, 40, and 80 ft in Figure 3). This configuration yielded a measurement of incident pressure with a component of reflected pressure due to the charge height of burst (HOB).

The sensors used for this at these ranges were Kulite Semiconductor Products model XT-190 pressure transducers, which are piezo-resistive devices utilizing a full four-active-arm Wheatstone bridge (Table 2). The XT-190 is manufactured in ranges from 5-psi to 10,000-psi. The natural frequencies of the gage are very high, ranging from 70 kHz to 650 kHz for the XT-190 model. Signals from the transducers were amplified and recorded by a Hi-Techniques Me-DAQ. The digital recorders in the Me-DAQ have variable memory sizes ranging from 1k to 2M samples with 14-bit vertical resolution. Sample rates for this test were two microseconds per point with acquisition lengths of 1 mega sample resulting in a total record time of 2 sec.

The testbed was fitted with an array of 12 transducers in concrete mounts placed flush with the ground surface (Figure 4). The transducer mounts were placed as level with the ground as possible. The dirt surrounding the mounts was raked to provide a smooth area for shock-wave propagation. The cabling was trenched into the ground to protect it from fragmentation.

Figure 3. Radial layouts of pressure transducers (East, North, West Southwest). The red circle illustrates the shot location while the black circles represent the pressure transducer locations.

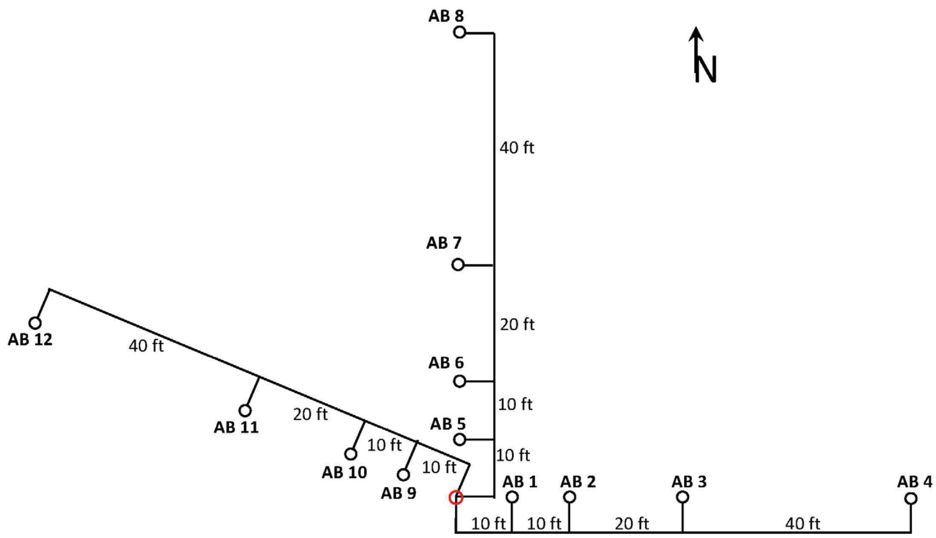

Table 2. XT-190 specifications and setup.

Meas #	Channel	SN	Range (PSI)	Excitation (volts)	Sensitivity (mV/V/PSI)	Scale Factor (PSI/V)
AB1	1	H48-17	200	9.93	0.065247	1543.5
AB2	2	F54-99	100	9.93	0.098313	1024.3
AB3	3	J48-9	25	9.94	0.201371	499.6
AB4	4	T60-32	10	9.93	0.995539	101.2
AB5	5	G62-3	200	9.94	0.049208	2044.5
AB6	6	Z59-56	100	9.94	0.099197	1014.2
AB7	7	F61-48	25	9.95	0.373826	268.8
AB8	8	F47-5	5	9.92	1.281033	78.7
AB9	9	P21-45	200	9.86	0.082219	1233.5
AB10	10	Q60-75	100	9.94	0.097440	1032.5
AB11	11	L61-72	25	9.95	0.369984	271.6
AB12	12	W28-55	10	9.93	1.664608	60.5

Figure 4. Pressure transducer mount (left) and installed mount (right).

2.3.2 Mid-field

Validynes (Model P55D) with no mechanical wind filters were installed in the mid-field area (transition range). They were located at distances of 30 m to 250 m from the source, as shown in Table 3. Figure 5 provides an overview of some of the mid-field instrumentation layout in relation to the source location.

The Validyne sensor is a compact differential pressure transmitter that is used for a wide variety of low-pressure measurements. The sensor specifications are listed in Table 4. These sensors were sampled at 1,000 samples per sec with a Reftek 125A digitizer set to gain x4.

Figure 5. Overview map showing the location of the three of the Validyne sensors, B030, B060, and B125, with relation to the shot location.

Table 3. The distance of the Validyne sensors used for the mid-field range.

Site	Distance from Source (m)
B030	30
B060	60
B125	125
B250	250

Table 4. The Validyne sensor specification.

Range	± 0.08 psid to ± 3200 psid
Accuracy	± 0.25% FS
Overpressure	200% FS to 4000 psi
Temperature Errors	± 0.5% FS
Frequency Response	Low Pass Filter at 250 Hz

2.3.3 Far-field infrasound sensors

The far-field was instrumented with an array of seven infrasound sensors, referred to as the Step Out Array (S1 – S7); the Denied Area Monitoring and Exploitation of Structures (DAMES) Array installed at ERDC; and three additional sensors at 8.4 km, referred to as the Instrumentation site. These sensors were Inter Mountain Laboratory (IML) model ST infrasound gauges. Most of these sensors were installed with porous hose wind filters. Table 5 provides sensor installation details (distance from source, sample rate, and wind filter type). Figure 6 provides an overview of the far-field instrumentation layout in relation to the source location.

Most of these sensors, including from the near- and mid-field range, are temporary sensors deployed for the experiment, while the DAMES Array is a permanent instrumentation location. The DAMES Array is a seismic-acoustic array installed on the ERDC Vicksburg campus and built as part of the Denied-Area Monitoring Using Infrasound (DAMUI) Center Directed Research Initiative. The DAMES array monitors sources and explosive testing testing at graduated distances, i.e., Mississippi River Bridges (3.7 km), Big Black Test Site (14.3 km), Fort Polk (247 km), and Eglin AFB (437 km). It is designed to be compatible to the Comprehensive Nuclear-Test-Ban Treaty infrasound array (1-km aperture tripartite) with an embedded small aperture array (60-m cross) at 14 km. This array has several other sensors but, for the purpose of this paper, the focus is on the IML sensors. Additional information on these arrays can be found in Swearingen et al. (2013).

Table 5. The IML sensors used for the far-field range.

Site Name	Distance From Source (km)	Sample Rate (Hz)	Wind Filter
S1	1.03157	1000	4- 50’ hoses
S2	2.061013	1000	4- 50’ hoses
S3	3.053574	1000	4- 50’ hoses
S4	3.968249	1000	4- 50’ hoses
S6	6.027629	1000	4- 50’ hoses
S7	6.984477	1000	4- 50’ hoses
Instrumentation	8.442056	500	4- 25’hoses (see Table 6)
DAMES	13.07734	500	4- 50’ hoses
DAMES	13.22054	500	4- 50’ hoses
DAMES	14.25398	500	4- 50’ hoses
DAMES	14.52298	500	4- 50’ hoses
DAMES	14.49208	500	4- 50’ hoses
DAMES	14.48418	500	4- 50’ hoses
DAMES	14.4993	500	4- 50’ hoses
DAMES	14.50855	500	4- 50’ hoses

2.3.4 Instrumentation site

Several sensors were deployed at the Instrumentation site for the purpose of investigating different types of wind-noise mitigation strategies. Three types of sensors were used in this study, i.e., Chaparrals, the IML sensors described in the previous section, and Hyperion infrasound sensors. The signals from these sensors were recorded with a sample rate of 500 Hz with three 6-channel REFTEK digitizers (Reftek 130-01/6). The nominal sensitivity of the three sensors are as follows, i.e., Chaparral – 3.9725 μPa/count (0.40 V/Pa); IML – 7.94 μPa/count (0.20 V/Pa); and Hyperion – 10.593 μPa/count (0.15 V/Pa).

Figure 6. Overview map showing locations of far-field instrumentation (Table 5) in relation to the shot location. The red circles represent 5, 10, and 15 km from the shot location.

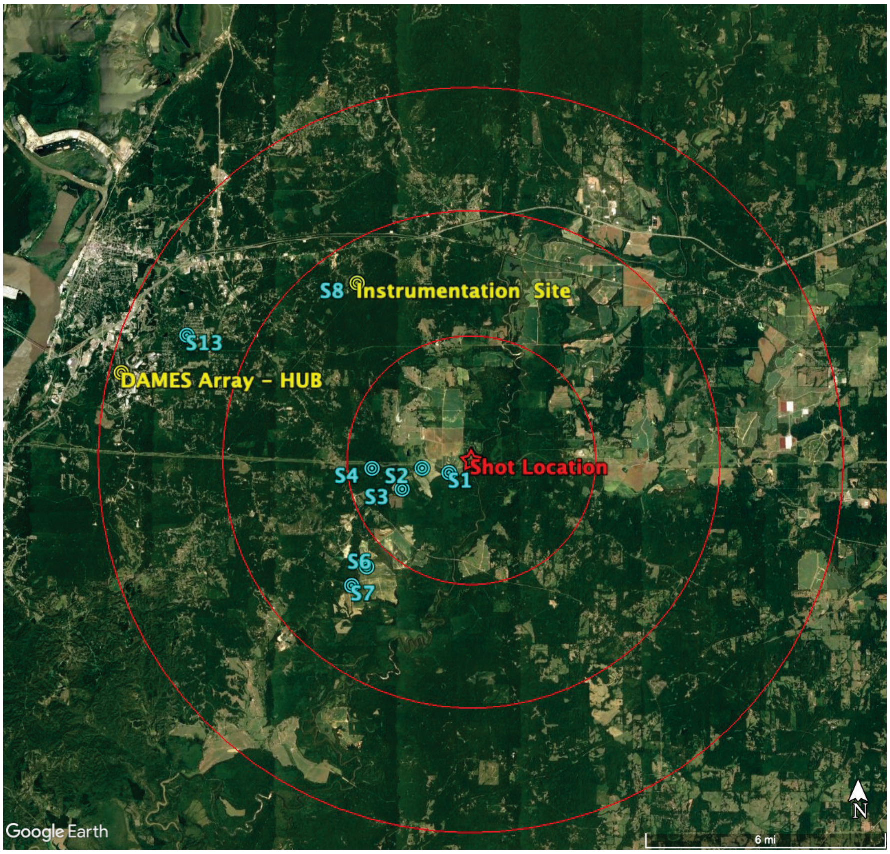

Several types of mechanical wind filters were investigated. These included three brands of porous hoses, i.e., Fiskar™, ColorRite™, and Westward™. The hoses were placed in various configurations including coiled, crossed, and with segments placed parallel and perpendicular to the estimated path of the acoustic wave. Different lengths of hoses were also investigated. Other types of wind filters included piling leaves, placing a pillow, and placing a bag of rocks over the sensor. The sensors are listed in Table 6 along with the digitizer label (with channel), and the type of wind filter used. As an example, Sensor 11 from Table 6 is an IML sensor with porous hoses in a cross pattern, as shown in Figure 7. As shown, four hoses, each 7.62 m (25 ft) long, were connected to the four sides of the sensor and laid out so that the aperture of the sensor was 15.24 m (50 ft). A photograph of the several of the sensors in the Instrumentation site is included in Appendix A. Notice the pile of leaves in the center of the photo, under which is located the Chaparral, Sensor 1 in Table 6.

Table 6. Sensors used in the Instrumentation site wind filter study.

Sensor #	Sensor Type	Digitizer – Chan #	Filter Type
1	Chaparral	A056 - 1	Buried in leaves
2	Chaparral	A056 - 1	Coiled 25 ft Fiskar hoses
3	Chaparral	A056 - 1	2 – 25 ft Fiskar hoses parallel to shot
4	Chaparral	A056 - 1	2 – 25 ft Fiskar hoses perpendicular to shot
5	Chaparral	A056 - 1	4 – 25 ft Fiskar hoses in a cross
6	Chaparral	A056 - 1	4 – 25 ft Westward hoses in a cross
7	Chaparral	A058 - 5	Pillow
8	Chaparral	A019 - 2	4 – 25 ft ColorRite hoses in a cross
9	IML	A019 – 3	Top removed
10	IML	A019 – 4	4 – 25 ft hoses
11	IML	A058 - 3	Short hose
12	Hyperion	A058 - 1	Papasan
13	Hyperion	A058 - 2	Bag of rocks

Figure 7. Example of an IML sensor with four porous hoses.

2.3.5 Microphones and geophones

Several geophones were installed at source-receiver distances (ranges) from 7 m to 8.434 km along with the sensors listed in the previous two sections. Five geophones were co-located with the Validyne pressure sensors. Eight geophones were installed at distances from 0.4 km to 2 km, between the Validyne array and the Instrumentation site, with broadband microphones also installed near these geophones. Figure 8 shows the positions of these sensors relative to the source. Table 7 contains a list of these sensors, along with their distance from the source.

Three geophones were installed at 0.5 km in an approximate right triangular array, also shown in Figure 8. A similar right triangular geophone array was installed at a distance of 2 km from the source. A three-element microphone array was installed near the NW geophone of each of these geophone arrays in an approximate right-triangle configuration. For the array at 500 m, the distances between the microphones were 1.28, 1.39, and 1.91 m. The configuration was similar at the 2-km location.

There were also microphones and geophones installed at the Instrumentation site. These included a 1-Hz 3-component (3C) geophone and a 4.5Hz 3C geophone and a 3-element microphone array. Figure 8 zoomed-in view shows the relative position of these sensors. The 3C geophones were oriented with axes oriented in the N-S, E-W, and vertical directions.

Figure 8. Top: Locations of Validynes, geophones, and microphones to distances of 2km from source; middle: Zoomed-in view of the geophone and microphone arrays at 0.5 km from source; bottom: Zoomed-in view of the microphone and geophones at the Instrumentation site, approximately 8.44 km from the source.

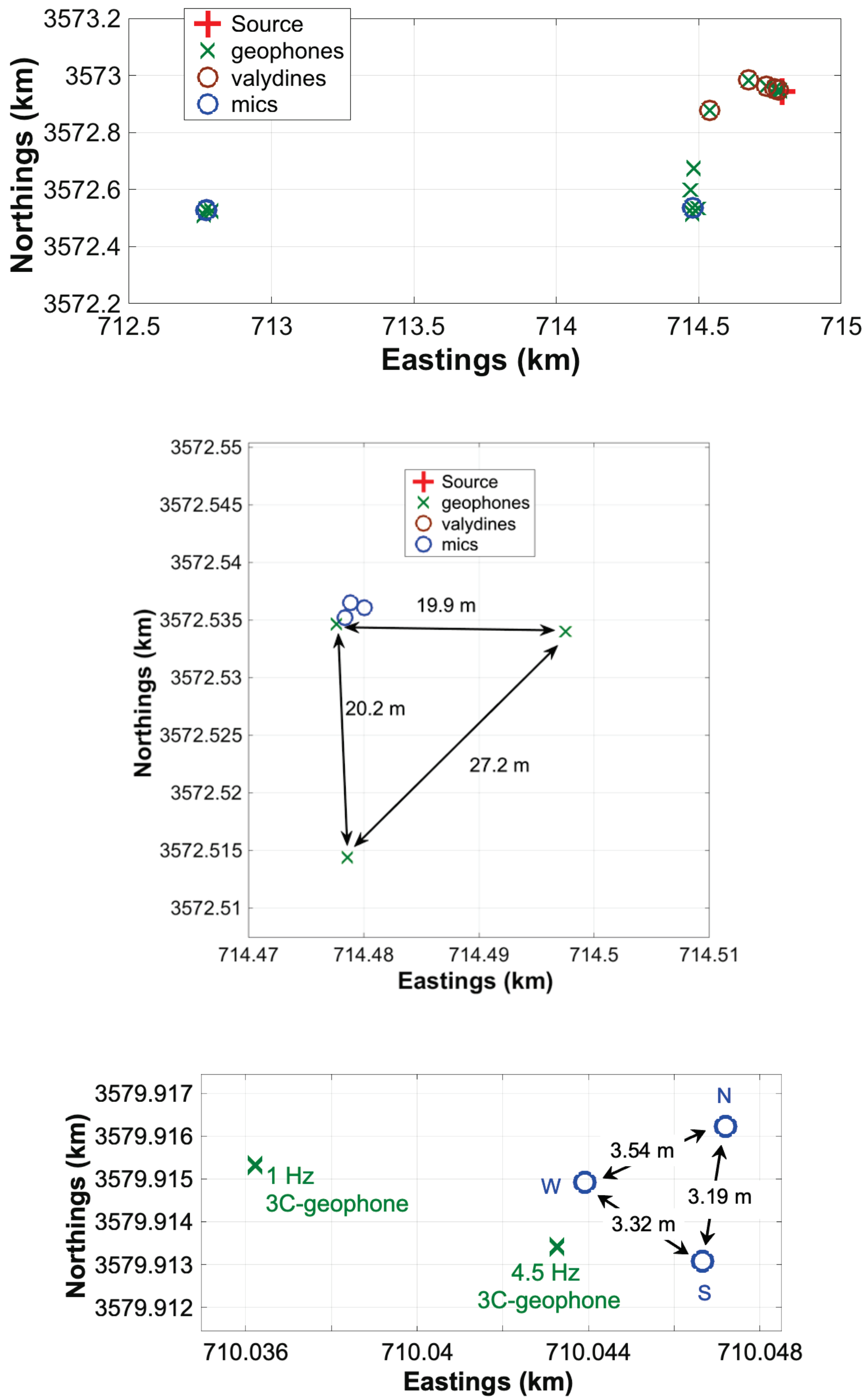

Table 7. Geophones and microphones from near-field to instrumentation array.

Sensor	Dist. from Source (m)	Notes
Vert. Geophone	7.45	Lone
Vert. Geophone	14.52	Near Validyne
Vert. Geophone	29.91	Near Validyne
Vert. Geophone	59.26	Near Validyne
Vert. Geophone	124.15	Near Validyne
Vert. Geophone	263.45	Near Validyne
Vert. Geophone	413.12	Lone
Vert. Geophone	473.66	Lone
Vert. Geophone	506.83	3-element array
Vert. Geophone	518.20	3-element array near mic array
Vert. Geophone	533.80	3-element array
Microphone	515.96	500 m array
Microphone	515.56	500 m array
Microphone	517.29	500 m array
Vert. Geophone	2076.15	3-element array
Vert. Geophone	2048.58	3-element array
Vert. Geophone	2066.44	3-element array near mic array
Microphone	2065.67	2000 m array
Microphone	2064.83	2000 m array
Microphone	2066.18	2000 m array
3C geophone	8439.03	1 Hz geophones – instr. site
3C geophone	8433.47	4.5 Hz geophone – instr. site
Microphone	8431.29	3-element array - instr. site
Microphone	8433.59	3-element array - instr. site
Microphone	8434.37	3-element array - instr. site

3 Analysis and Results

As mentioned in the previous chapter, the pressure waves associated with the explosions were recorded with three types of sensors with source-receiver spacing ranging from 3 m to 14.500 km. In the near-field at ranges less than 30 m, the shock waves had very sharp rise times to peak pressures on the order of 10^4 to 10^6 Pa. For the majority of the mid-field region, the range from 30 to 300 m, the instrumentation clipped the observed signals because the amplitude of the shock waves exceeded the dynamic ranges of the sensors (see Table 4), especially for the larger shots. Therefore, the peak pressures were unable to be determined. However, the signals in this region started to resemble acoustic pulses with a positive peak immediately followed by a negative peak.

The far-field region sensors, ranges 1 to 14.5 km, used porous hoses as wind filters and, thus, had a sizeable spatial aperture. Although this abated the ambient noise due to the wind, the wind filters affected the frequency and amplitude responses of the recorded signals. Even so, accurate measurements of the time of arrival (TOA) of the different signals were made.

3.1 Shock wave

The pressure-time series were recorded for all 12 measurement locations on all five tests. The time series for shots 1 and 4 recorded at 3.05 and 12.19 m (10 and 40 ft, actual measurements made in units of feet and converted to metric), respectively, are plotted in Figure 9. Within this range, the pressure wave has a very fast rise time. A second peak can be seen in shot 4. These are believed to be ground reflections. The BlastX code (ERDC 2001) estimates of peak pressure for shots 1 and 4, as a function of range (distance from the source) are plotted in Figure 10 alongside the measured peak pressures. This figure shows that the pressure amplitude decays almost linearly with distance on a log-log plot.

Figure 9. Shock waves from shots 1 and 4 recorded with the Kulite pressure transducers. Top left – shot 1 at 3.05 m; top right – shot 1 at 12.19 m; bottom left – shot 4 at 3.05 m; bottom right – shot 4 at 12.19 m.

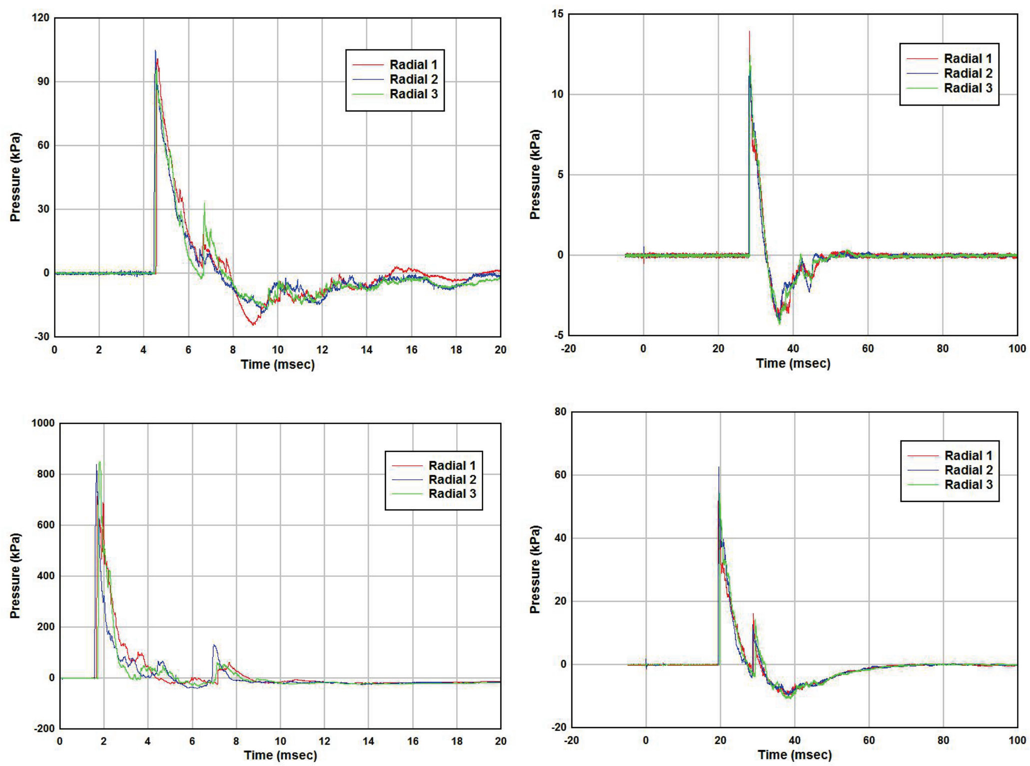

3.2 Propagation

The peak amplitude decays dramatically with range as the pressure wave propagates away from the site of the explosion. This is demonstrated in Figure 11, which shows the signals recorded from shot 4 with the step out array, sensors S1 through S7. The signals recorded with S1 and S2 appear to be clipped.

The positive peak amplitude from all the shots was then plotted as a function of range as shown in Figure 12. The dashed line, which intersects the point representing the peak amplitude of shot 5 at the 3-m range, represents spherical spreading. The text box with arrows identifies the signals that were clipped, i.e., the dynamic range of the sensor was not sufficient to record the highest amplitudes of the pressure wave. All of the mid-field sensors clipped in shot 4, and two of them, located at 30 and 60 m, clipped in shot 3. The signals from all of the shots were clipped by the nearest far-field sensor, S1 at 1 km. The far-field sensor at 2 km, S2, was clipped for all but the smallest shots. Other than those signals that were clipped, the largest peak amplitudes corresponded to shot 4, which is not surprising since this was the largest charge.

Figure 10. BlastX predictions plotted alongside measured peak pressure as a function of distance from the source. The top plot is for shot 1; bottom plot is for shot 4.

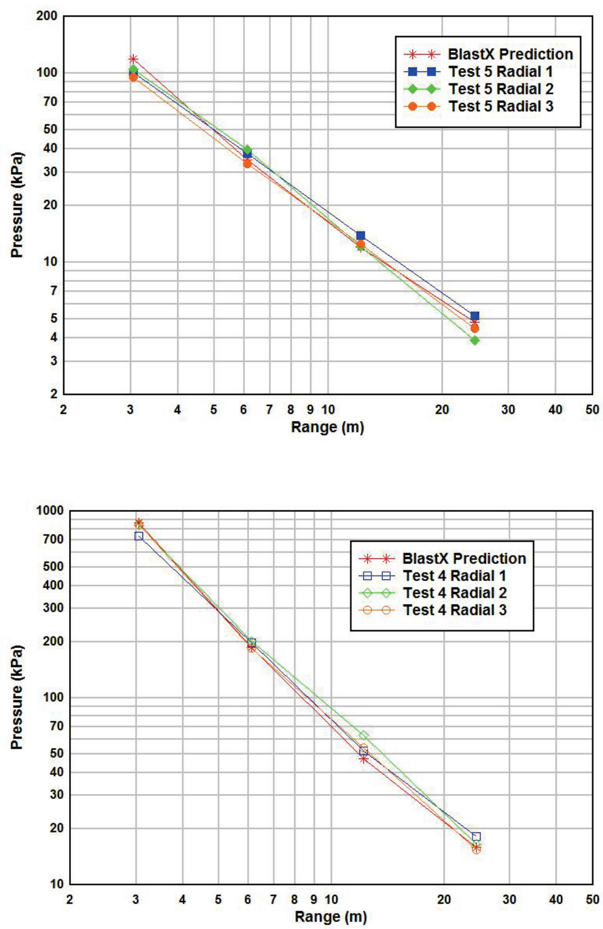

Past researchers developed models that relate the peak amplitude to the scaled distance, which is the distance from the source divided by the cube root of the mass of the explosive (Pater 1981; Kingery and Bulmush 1984).

$$P_M = C\left(\frac{R}{W^{1/3}}\right)^{\propto} \quad (2)$$

where P_M is the scaled pressure, R is the range, and W is the mass of the explosive. The constants C and α are essentially constant in the mid-field and far-field, but not in the near-field. The case where α = -1 represents the spherical expansion without attenuation in a homogeneous medium, i.e., spherical spreading or peak amplitude inversely proportional to range.

Figure 11. Time series associated with shot 4 for all sensors in the Step Out Array.

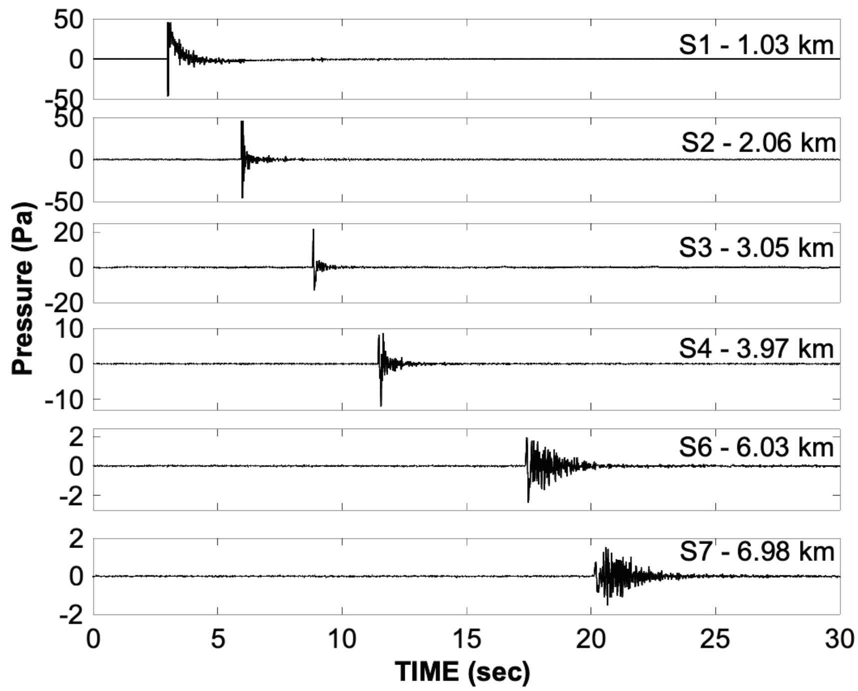

The data shown in Figure 12 are plotted again in Figure 13 alongside the model represented by Equation 2. The signals that clipped were excluded from the plot. The model was fitted to the data qualitatively using the constants shown in the figure. The exponent α = -1.35 accounts for the attenuation associated with the upward refracting atmosphere in first 1 km or so above ground level, discussed in Section 2.2.

The model agrees well with the data corresponding to scaled distances from 10 to 1000 m/kg$^{1/3}$. This corresponds to data from the far near-field, with sensors located at 12.19 m for shot 2, 24.38 m for shot 4, and for the entire mid-field range. The fit was not as good in the nearer ranges, because the upward refracting atmosphere is negligible at these ranges.

The peak amplitudes in the far-field fall below the model curve. These signals were recorded with IML connected to porous hose filters. These sensors have a spatial aperture of 30 m, which contributes to the reduction in wind noise because of spatial averaging. In addition, the hoses contribute to insertion loss, i.e., a reduction in amplitude. It is interesting to note that the points from a given shot roughly follow a trend for values of

Figure 12. Peak amplitude as a function of source-receiver spacing.

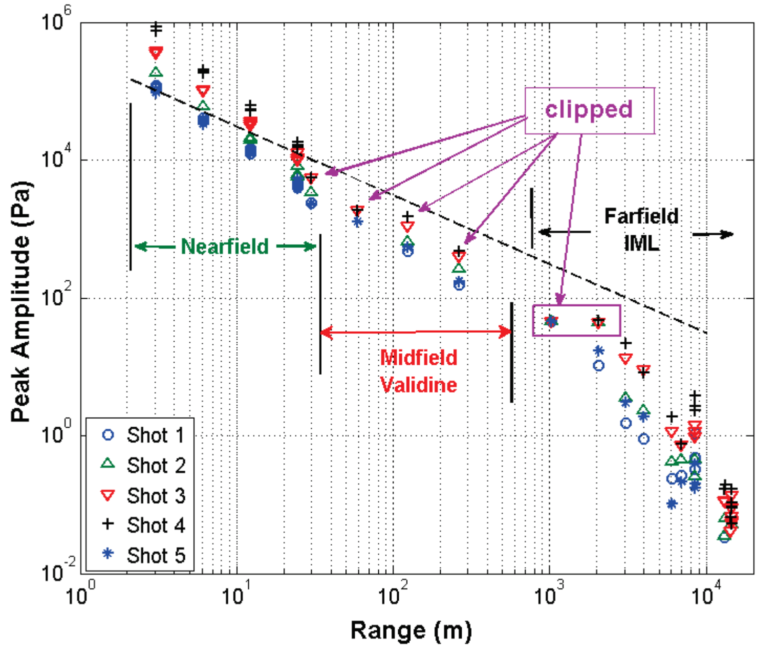

Figure 13. Peak amplitude, in decibels, versus scaled distance.

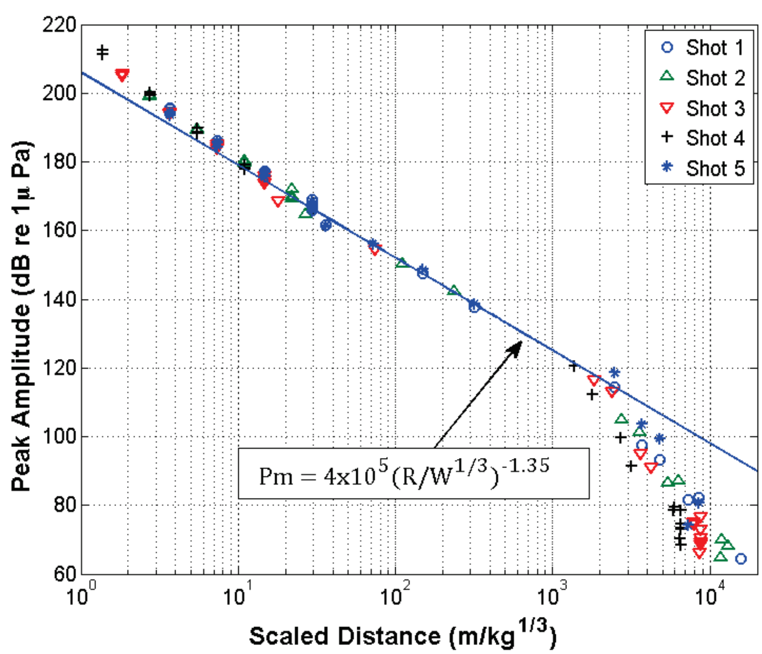

the scaled distance greater than 10^3. For instance, the values of peak amplitude lie below the other values, out to a scaled distance 6 x 10^3. The points beyond this scaled distance represent the signals recorded with the IML sensors at the 13 to 14.5 km range, as listed in Table 5. Rather than following the same trend as the preceding four points, these points line up vertically on the plots representing a 10 dB variation in peak amplitude for a small change in scaled distance. This is probably because these signals are close to the maximum detection range for these conditions.

3.3 Time of arrival

The time of arrival (TOA) of each signal was identified as the time associated with the first positive peak. In the cases in which the signal clipped, the TOA was recorded at the top of the first rise. The TOA was ambiguous for many of the signals recorded by sensors at the ranges greater than 13 km.

The TOAs for the near-, mid-, and far-field sensors from shot 4 are plotted in Figure 14. Upon careful inspection it can be seen that the points associated with the near-field sensors are not aligned; a curve through the points would change its slope because the shock wave near the source travels significantly faster than the speed of sound. This will be discussed in more detail in the following paragraph. In addition, the points corresponding to the mid-field TOA do not quite line up with the near-field and far-field points; this is especially true for the point at 30 m.

Figure 14. TOA versus range for all sensors at shot 4.

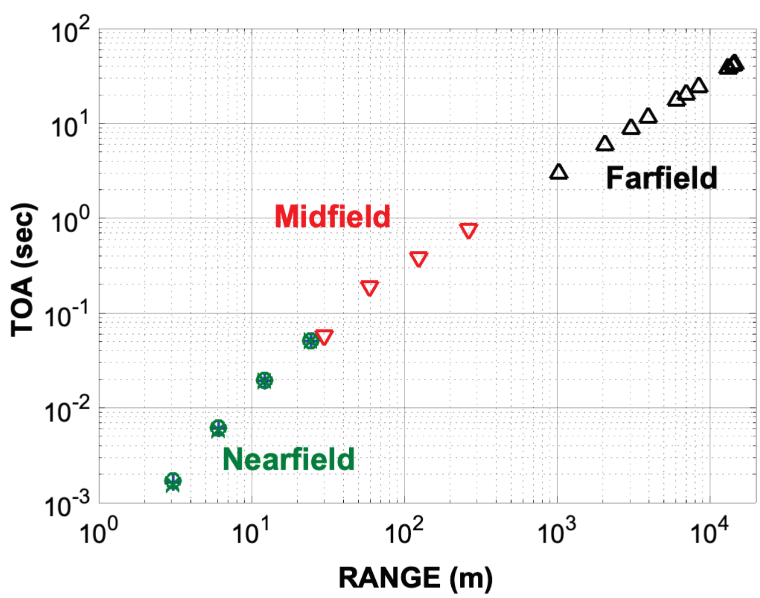

The TOA from the near-field sensors from shots 4 and 5 are plotted in Figure 15. The curvature is more pronounced in this figure, plotted on a linear scale, than in Figure 14. In Figure 15, the inverse slopes of the lines connecting the points represent the speed of the pressure wave, which shows that the speed decreases with range, agreeing with theory. Another observation from the data, as expected, was that the speed of the pressure front associated with shot 4, which was 10.9 kg, was significantly faster than the speed associated with shot 5, which was only 0.6 kg. It can also be seen that the speed of the shock wave was significantly faster at ranges nearer to the source; e.g., for shot 4 the shock speed was over double that of the speed of sound.

The TOAs from all far-field sensors from shots are plotted in Figure 16. The line in the figure is a least-square regression fit for all the points in the plot. The correlation coefficient shown in the figure is very close to one, indicating a good fit to the data. The inverse of the slope of this line, 345 m/s, is very close to the speed of sound at normal temperature and pressure, 343 m/s, which suggests that by the time the pressure wave is at these ranges, it has transitioned to an acoustic wave in the linear regime.

It was not possible to estimate the exact range at which this transition occurred because the TOA values from the mid-field sensors were suspect. The digitizers used with these sensors did not have a GPS clock. Although they were synchronized with a GPS prior to the test, it is suspected that the clocks drifted during the test. Some of the values determined from these sensors were less than 300 m/s, which is not credible.

Figure 15. Time of arrival (TOA) versus range for the near-field sensors for shot 5 (top) and shot 4 (bottom).

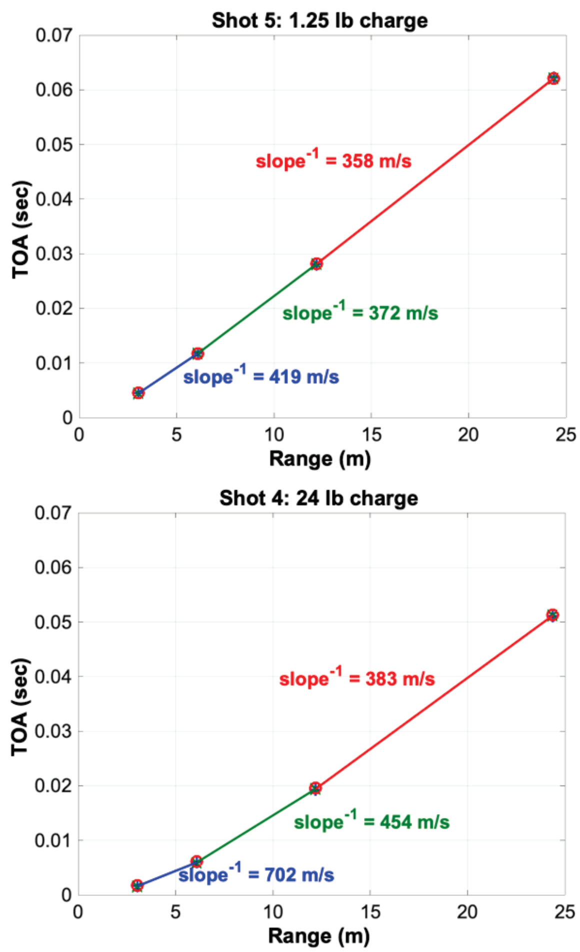

Figure 16. TOA versus range for the far-field sensors from all shots.

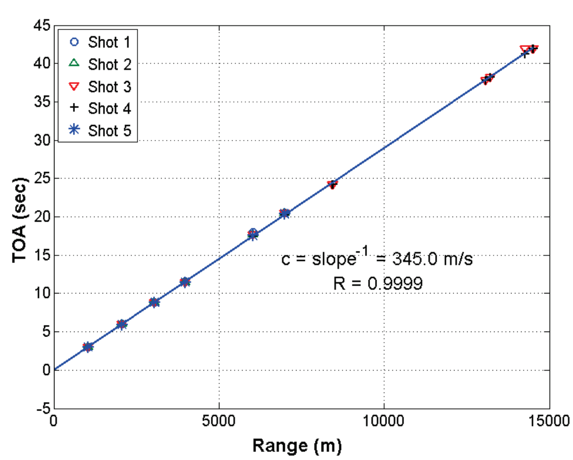

3.4 Wind filter analysis

Several sensors were deployed at the Instrumentation site 8.44 km from the shot location as described in Section 2.3.4 in order to evaluate the effectiveness of different wind filters. The sensors are listed in Table 6 along with the types of wind filters used. As mentioned in that section, three types of infrasound sensors were deployed, i.e., Chaparrals, IMLs, and Hyperion infrasound sensors. Eight Chaparrals are listed in Table 6. A ninth was deployed, channel 1 on digitizer A019, but it is not listed because no signal was observed, and the noise level was very low. It was deployed with WestWard hoses in flex conduit. Signals were also recorded with Valydine and Setra sensors, but they are not shown either because the signal amplitudes recorded with them were very low. Hoses 7.62 m (25 ft) in length were connected to several of the sensors. (Hoses were measured in feet and converted to meters.) With hoses connected to four sides of the sensor, the aperture of the sensor was 15.24 m (50 ft). Spatial averaging over a wider aperture attenuates the signal as the frequency increases (Walker and Hedlin 2010). If one assumes that sensors would be more sensitive to wavelengths greater than twice their aperture when oriented parallel to the direction of propagation of the acoustic wave, the effective band for these sensors would correspond to frequencies below 11 Hz.

The acoustic signal from the shots took about 24 sec to travel to the site. Figure 17 shows 40 sec of the signals recorded with the Chaparrals, IMLs, and Hyperion sensors, starting at the time the shot 2 was detonated, i.e., wire break. No digital filters were applied to these signals. An offset was added to the signals in order to separate them for clearer viewing. The transient waveform produced by the pulse can be seen on most channels in the figure. With this zoomed out of view, it can be seen that some of signals are very noisy, particularly that associated with Sensor 4, which, according to Table 6, is connected to Fiskar hoses perpendicular to shot. The authors suspect that the seals on this sensor had gone bad.

A zoomed-in view of the same signals are plotted in Figure 18. The figure shows that the signals recorded with sensors 1 and 2 are very small or undetectable. Sensor 1 was buried in leaves, and sensor 2 was connected to a coiled Fiskar hose. The signal associated with sensor 4, which is seen to be very noisy in Figure 17, has a much larger amplitude. The signals recorded with sensors 3, 5, 6, 7, and 8 are similar in amplitude and shape. The signals recorded from shot 2 with the IML and Hyperion sensors are also plotted in Figure 18. They also have similar amplitudes to each other, except for sensor 12, which is smaller in amplitude, persists for a longer time, and contains higher frequency content. This sensor was covered with a papasan but is suspected to not be functioning properly. The signal recorded with sensor 11 has an opposite polarity from the others, suggesting that the wires were switched. The zoomed-in view of signals recorded with all sensors and all shots are plotted in Appendix B.

Figure 17. Top: Signals recorded from shot 2 with the Chaparral sensors. Bottom: Signals recorded from shot 2 with the IML and Hyperion sensors. The numbers in the legends correspond to the Sensor numbers in Table 6.

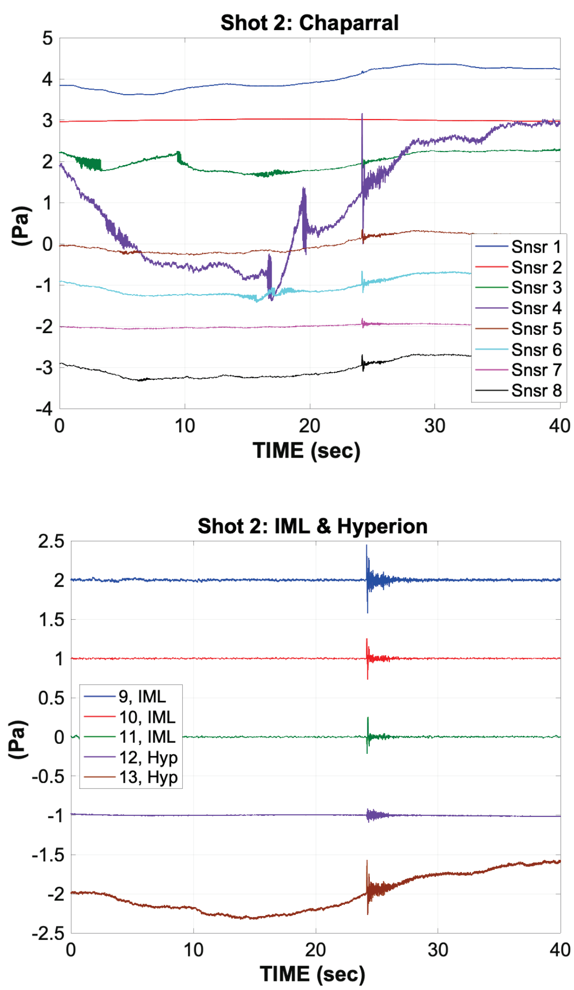

Figure 18. Top: Signals recorded from shot 2 with the Chaparral sensors. Bottom: Signals recorded from shot 2 with the IML and Hyperion sensors. The numbers in the legends correspond to the Sensor numbers in Table 6.

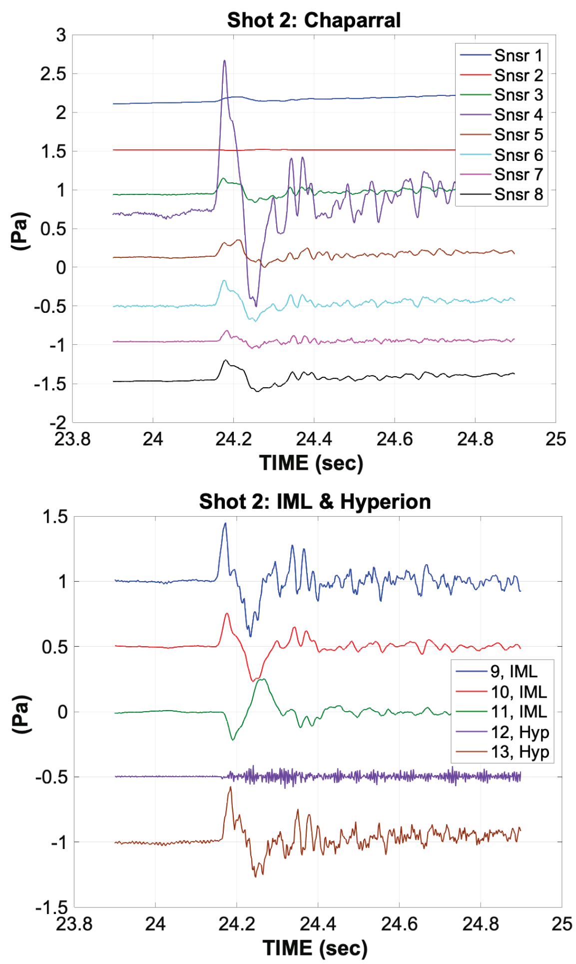

The power spectra of the background noise are plotted in Figure 19. The spectra were calculated over 5-min. periods before the first shot (16:20 – 16:25 UTC) and after the last shot (17:45 – 17:50 UTC). The spectra were calculated with the PWelch algorithm using 5,000 sample windows representing 10 sec. A Hamming window was applied to each of the windows. The signals were overlapped by 50% and padded to 10,000 samples.

It can be seen that the background noise corresponding to sensor 4 is very high, almost 20 dB higher than the next noisiest sensors (sensors 1,3, 5, and 8) but it was also seen to be noisy in Figure 17. It was mentioned that the seals on this sensor were probably bad. The background spectra corresponding to sensor 2 is very low, but the signal corresponding to this signal is very small, as is the signal from sensor 1, as seen in Figure 18. The background noise of the Hyperion under the papasan filter, sensor 12, is very low (Figure 19). As mentioned previously, the signal recorded with it appears to be distorted, which is evidence that the sensor may be faulty. Among the IML and the other Hyperion sensors, the background noise is similar from about 2 Hz to 20 Hz. Other than sensor 13, which corresponds to the Hyperion in the bag of rocks, the noise level below 2 Hz is very low. There is no significant difference in the background noise levels before and after the experiment.

Figure 19. Background noise recorded with the Chaparral, IML, and Hyperion sensors listed in Table 6. Top: Background noise before the first shot. Bottom: Background noise after last shot.

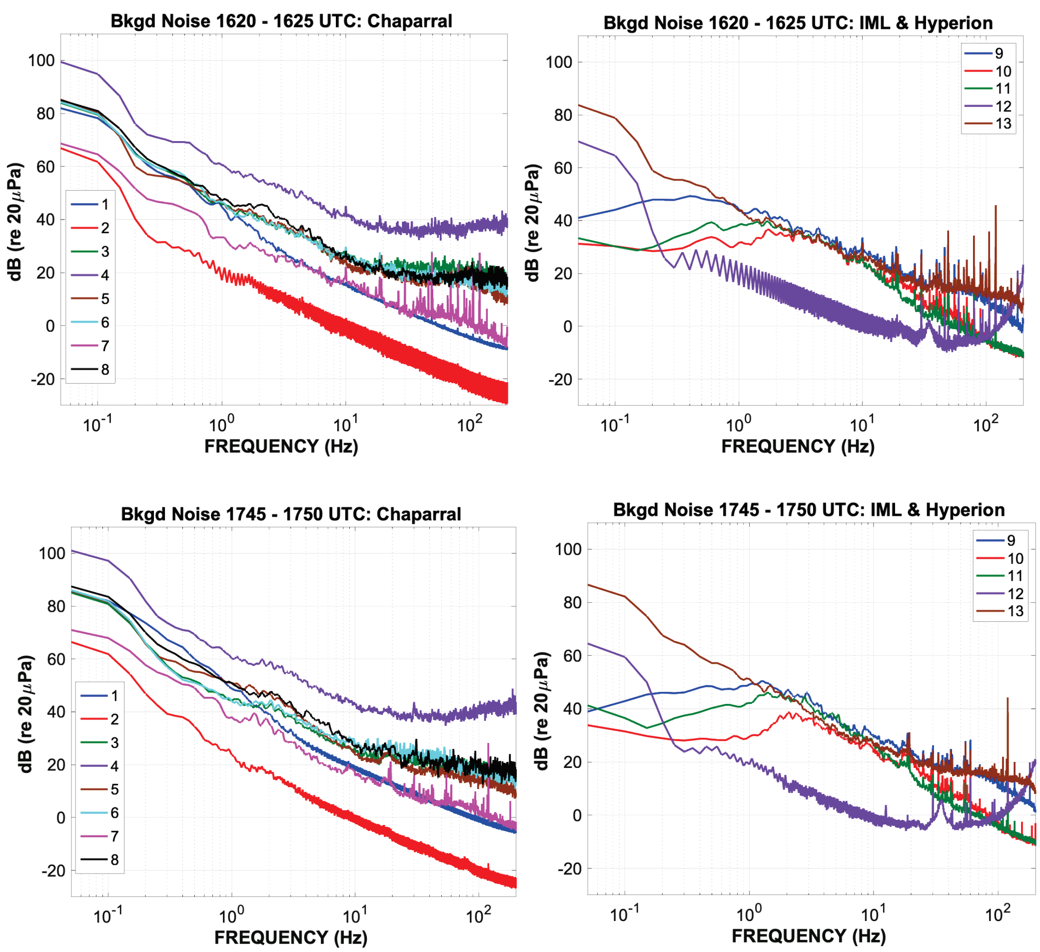

The signal-to-noise ratio (SNR) was determined for signals recorded by the sensors in Table 6. The energy spectra was calculated for the 1-sec windows shown in Figure 18. These spectra were calculated from the squared magnitudes of the Fast Fourier Transform (FFT) calculated over the 1-sec windows. This function of frequency was divided by the averaged background noise spectra, as shown in Appendix C. These background spectra were calculated from the squared magnitudes of the FFTs calculated over ten 1-sec windows from 1 to 11 sec as seen in Figure 17 and then averaged as a function of frequency. The results of these calculations, performed for shots 2 and 4, are shown in Figure 20. The difference between the two shots is mainly seen in the frequencies below 30 Hz; the SNR is considerably larger for shot 4 and exceeds 30 dB in this frequency band for many of the sensors. Above 30 Hz, the SNR is generally below 20 dB for both shots and all sensors, except for sensor 12, the Hyperion under the papasan, which is suspected to be bad. The SNR for all sensors and all shots are plotted in Appendix D.

Figure 20. Top left: SNR calculated from shot 2 with the Chaparral sensors. Top right: SNR calculated from shot 2 with IMLs and Hyperions. Bottom left: SNR calculated from shot 4 with Chaparral sensors. Bottom right: SNR calculated with the IML and Hyperion sensors from shot 4. Numbers in the legends correspond to the Sensor numbers in Table 6.

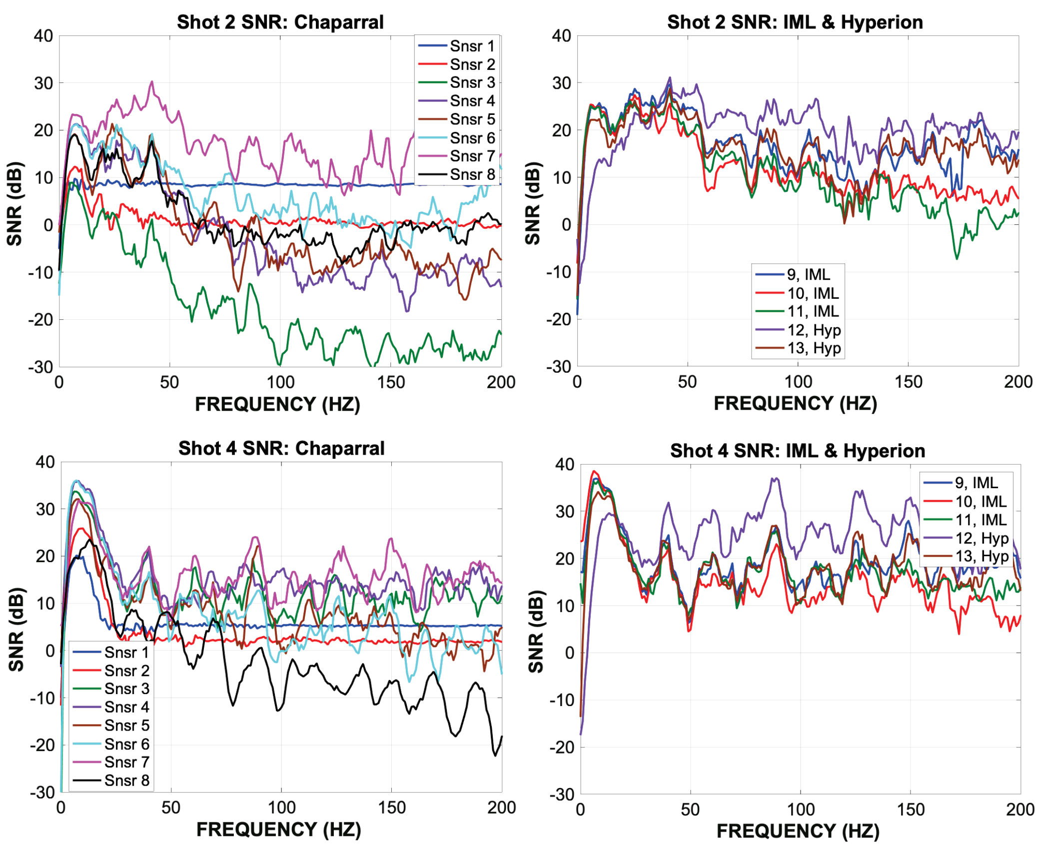

The Hyperion sensor under the papason (12) has a lower SNR than the rest of the sensors at low frequencies and a higher SNR at the higher frequencies. The other Hyperion and the IMLs perform similarly to each other. The Chaparral under the pillow (7) has a higher SNR than the others for shot 2, but not for shot 4. The Chaparral buried in leaves (1) has a constant SNR of under 10 dB, except for shot 4 where it bumps up to only 20 dB at frequencies under 20 Hz; it's as if the leaves smothered the sensor. The best performers for the Chaparrals appear to be sensors 4, 6, and 7, connected to hoses perpendicular to shot and in a cross, and placed under a pillow. Sensor 3 was not consistant, performing well for shot 4 but not 2.

Three Chaparrals were connected to hoses from different manufacturers, but in similar configurations: sensors 2 5, 6, and 8. They all respond similarly to background noise as shown in Figure 19. When considering SNR, sensor 6 outperforms the other two in shot 2. In shot 4, sensors 5 and 6 perform similarly while the SNR corresponding to sensor 8 is considerably lower.

3.5 Acoustic seismic coupling

As discussed in Section 2.3.5 and listed in Table 7, seismometers, or geophones, were installed with source-receiver distances from 7 m to 8.4 km. As shown in Figure 8, some of these were located in the vicinity of broadband microphones. In addition, as mentioned in that section, some of the geophone sites were comprised of 3C arrays. This deployment of geophones allowed us to consider four questions: (1) How far can the seismically coupled shock wave be detected from the source? (2) How well does the airborne shock waves recorded with geophones, i.e., acoustically coupled seismic wave, compare with the signals recorded with microphones? (3) Can the direction of arrival (DOA) of the airborne shock wave be accurately determined from differences in arrival times from an array of vertical geophones? and (4) Can the direction of arrival (DOA) of the airborne shock wave be accurately determined from a 3C seismometer or geophone? These questions will be considered in this section.

3.5.1 Direct seismic coupling

Seismic signals from the explosions coupled directly to the ground at ground zero and propagated seismically to the sensors through the ground, as observed by Albert et al. (2013). The seismic arrivals were not observed for ranges less than 30 m since the shock wave in air overwhelmed these signals, but were clearly observed at 30, 60, and 125

m. The signals recorded with the geophone installed at 260 m were relatively noisy, and the seismic arrival was not observed above the noise level. The next closest geophones were at ranges of over 400 m, and no arrivals were observed with these sensors either. These source-receiver spacings for seismic arrivals are consistent with those observed by Albert et al. (2013). The time-series waveforms showing the three seismic arrivals for shot 1, which is one of the smallest shots, are plotted in Figure 21 for the sensors mentioned above.

Also shown in Figure 21 are the times of arrivals and the peak amplitudes of the seismic arrivals for all five shots. The peak amplitude was greatest for shot 4 and least for shots 1 and 5; these were the tests with the largest and smallest charges, respectively. The results for shots 1 and 5 show that the results were repeatable since these charges were the same size. The size of the charge did not affect the times of arrival of the seismic waves as it did with the airborne shock waves, as discussed in Section 3.3.

Figure 21. Top: Time series waveforms of seismic arrivals for sensors at 30, 60, and 125 m. The time series is cut off at the time just before arrival of the air shock, which overwhelms the vertical scale; middle: Times of arrival for all 5 tests corresponding to these same sensors; bottom: Peak amplitudes for all 5 shots.

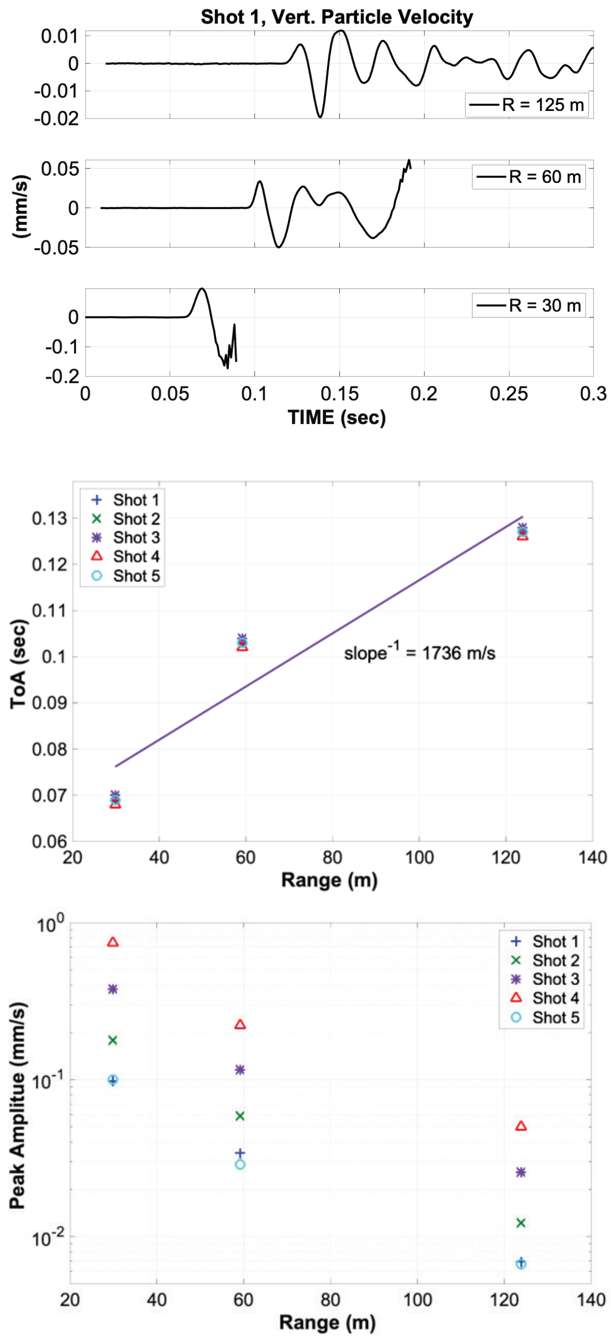

3.5.2 Seismic coupling of airborne shock

The geophones also recorded the acoustically coupled seismic signals associated with the passage of the airborne shock waves and acoustic waves. The time-series waveforms corresponding to shot 3 are plotted in Figure 22. The times of arrival of the geophone detected air shock wave for all five tests are plotted in Figure 23. The slope of the least-squares fit on arrival plots indicates that the shock wave in air travels much more slowly than the seismic wave. This speed compares favorably to that determined with the acoustic sensors, as discussed in Section 3.3 and depicted in Figure 16.

The absolute value of the amplitude (magnitude) of the largest negative peak of the shock waves as measured with the geophones are plotted in Figure 23. The two closest geophones, at distances of 7 and 15 m from the source, were buried to a depth of approximately 1 m in order to protect them from the blast wave. This probably accounts for the lower magnitude signal recorded with these sensors. It is also important to point out that the amplitudes of the airborne shock waves have much larger amplitudes than the seismic waves, and the amplitudes corresponding to ranges of 263 to 534 m are much smaller than those corresponding to 2,072 and 8,434 m. The latter is probably an indication that there is an error in converting from digitized values to engineering units. Also, most of the geophones used for this test were not calibrated for the test. The sensor at 8,440 m is a 1-Hz seismometer with a different sensitivity and not included in this figure.

The coherence function is a non-negative number less than or equal to one. The function equals one if the signals recorded by the sensors are linearly related and equals zero if they are not linearly related. Acoustic signals recorded with microphones are generally accepted as accurate representations of pressure signals at the point they are located. A coherence between a microphone and a nearby geophone that is equal to or nearly one, within a certain frequency band, would indicate that the waveform measured with the geophone was a reasonable representation within this band. In other words, it indicates that the phase information is preserved by the geophone (Shin and Hammond 2008).

Figure 22. Time series waveforms of shock arrivals for shot 3, recorded by geophones ranging from 7 m to 8440 m from source.

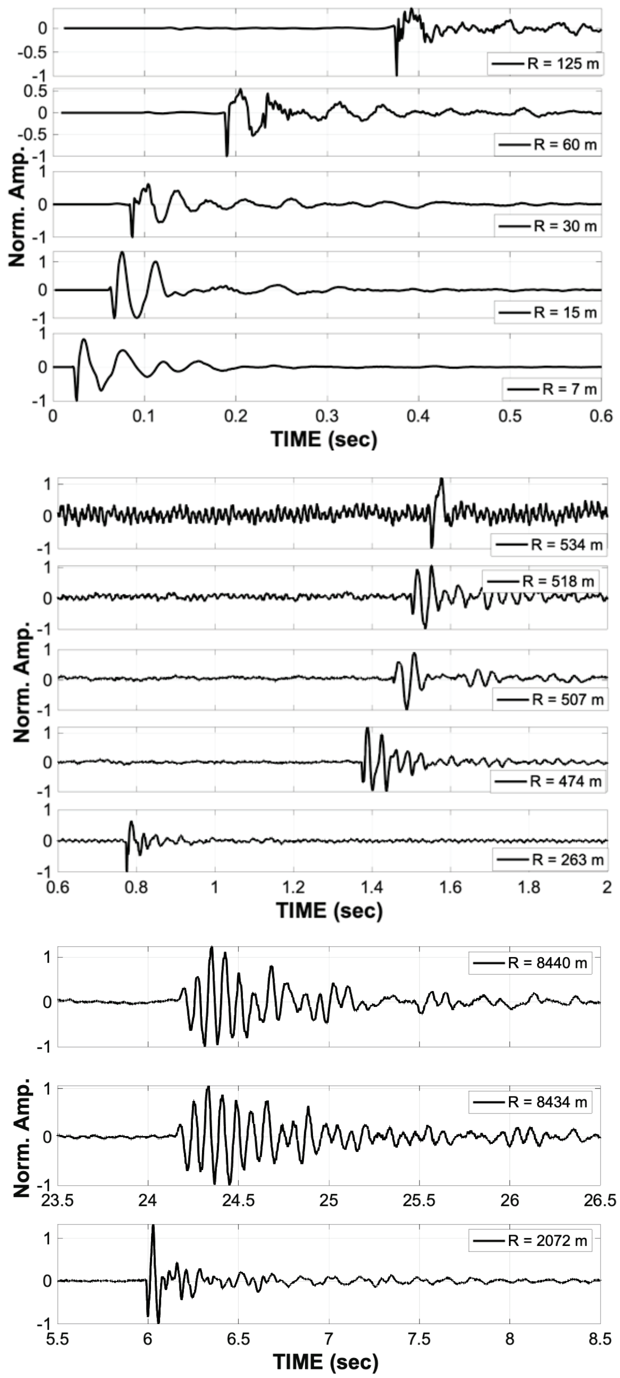

Figure 23. Top: Time of arrival of shock wave as recorded with geophones. The line represents a least-squares fit to the data. Bottom: Magnitude of negative peak of shock wave as recorded with geophones.

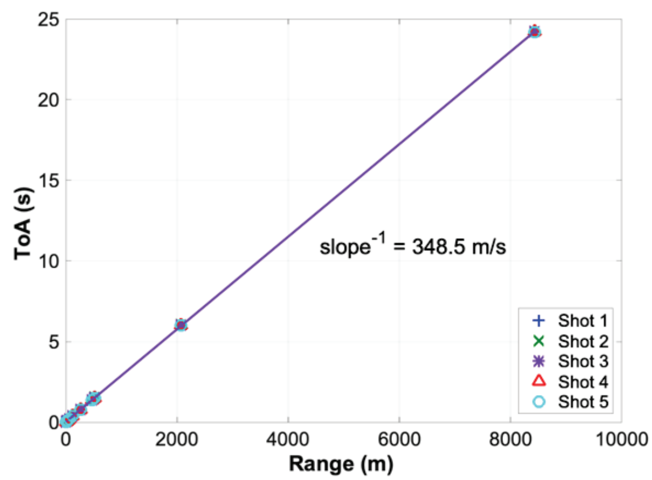

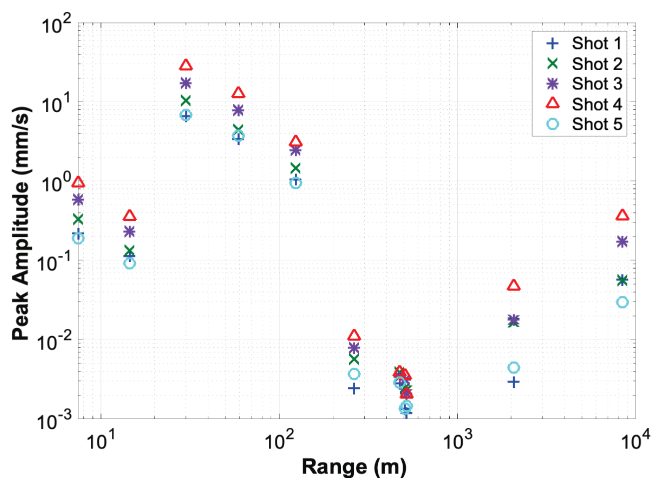

The coherence between the microphone and geophone signals was determined for three sites, i.e., microphones at 516 m, 2,066 m, and 8,434 m distance from the source. The corresponding geophones were located within meters from the microphones at 508, 2,072, and 8,434 m. The signals recorded with these sensors from shot 3 are plotted in Figure 24. The results of the coherence calculations are plotted in Figure 25. They show that the geophone and microphone signals are coherent for frequencies from less than 20 Hz to 50 Hz for the 516-m case and from 3 Hz to 50 Hz for the 2,070-m case. The coherence at 8,434 m is not nearly as good at frequencies below 40 Hz, being only from 8 to 20 Hz, probably because the signal amplitudes and SNR are much lower at this range. However, this plot shows that there is coherence in the signal at 40 Hz and above.

Figure 24. The acoustic arrival recorded from shot 3 with geophones and microphones located at the ranges indicated.

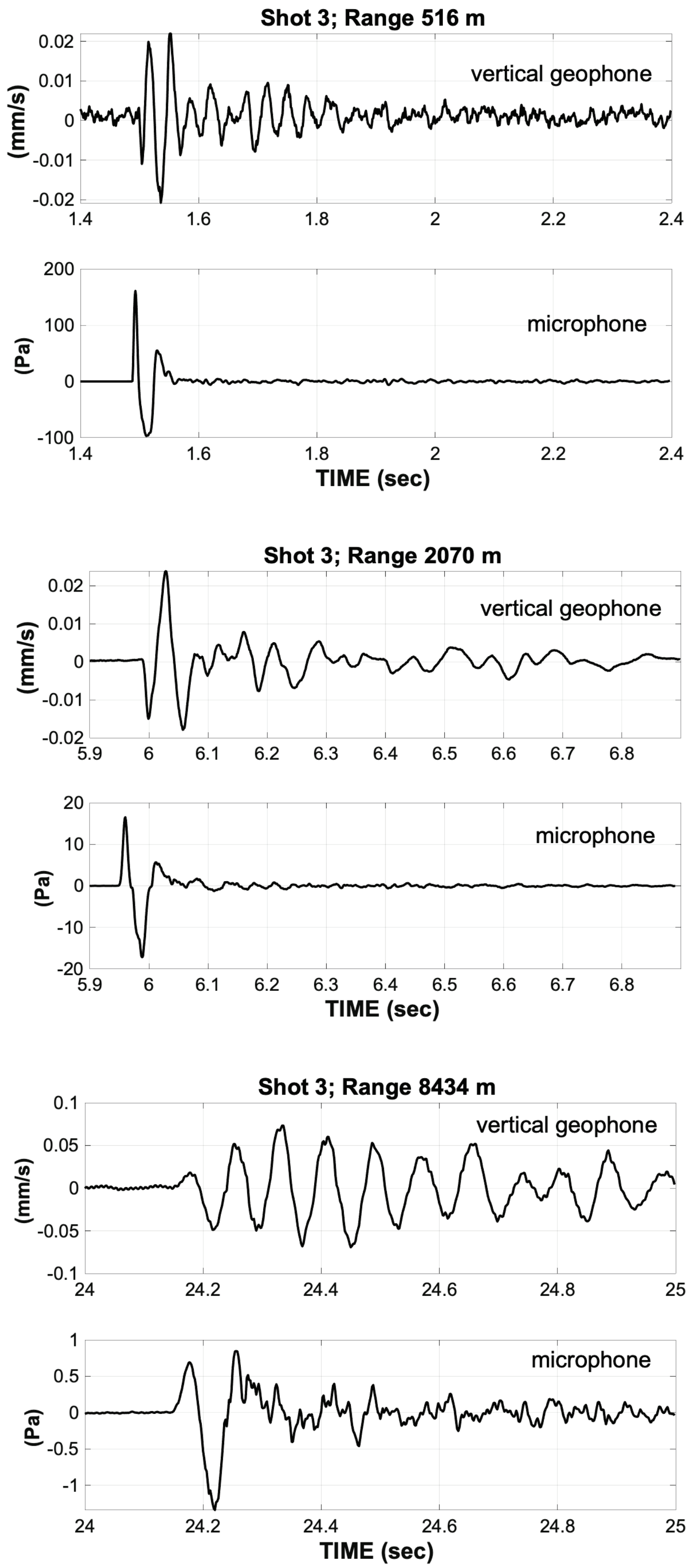

As a check, the coherence calculation was performed on segments of this time series not containing the transient pulse associated with the acoustic wave, i.e., periods of background noise. The results showed poor coherence between the geophone and microphone signals, which is evidence that the coherence between the sensors at 8,438 m, shown in Figure 25, is associated with the acoustic wave produced by the explosion and not other sources, such as noise or wind.

The acoustic-seismic coupling coefficient, referred to here as the transfer function, was calculated between particle velocity as measured with the geophone and the acoustic pressure as measured with the microphone. These results are plotted in Figure 26 alongside the coherence. The transfer function has units of (μm/s)/Pa, which is the inverse of specific acoustic impedance. The calculation was made by calculating the fast-Fourier transform (FFT) of the microphone and geophone signals from each shot. The same time windows were used as shown in Figure 24. The FFT of the geophone signals was divided by the FFT of the microphone, which results in complex functions of frequency. The plots in Figure 25 represent the magnitudes of these complex functions.

It is interesting to note that the transfer functions between shots at the same source-receiver separation show good agreement at frequencies in which the coherence is close to one. In regions outside this agreement, it is not good at all. In addition, there is not good agreement in the value of the transfer functions at the different ranges. The discrepancies in the amplitudes at 518, 2,072, and 8,434 m, as observed in Figure 24, obviously contribute to this. Also, the microphones and geophones were not exactly collocated and were actually several meters apart in some instances. Even with these shortcomings, these results demonstrate that geophones can provide adequate representations of acoustic waves as long as there is suitable SNR.

Figure 25. The transfer and coherence functions between acoustic signals from the explosion recorded with microphones and geophones at three distance from the source: top – 516 m; middle – 2,070 m; bottom – 8,434 m. The red dots on the curves indicate points for which the coherence is greater than 0.9. The numbers in the legend at top indicate the shot number.

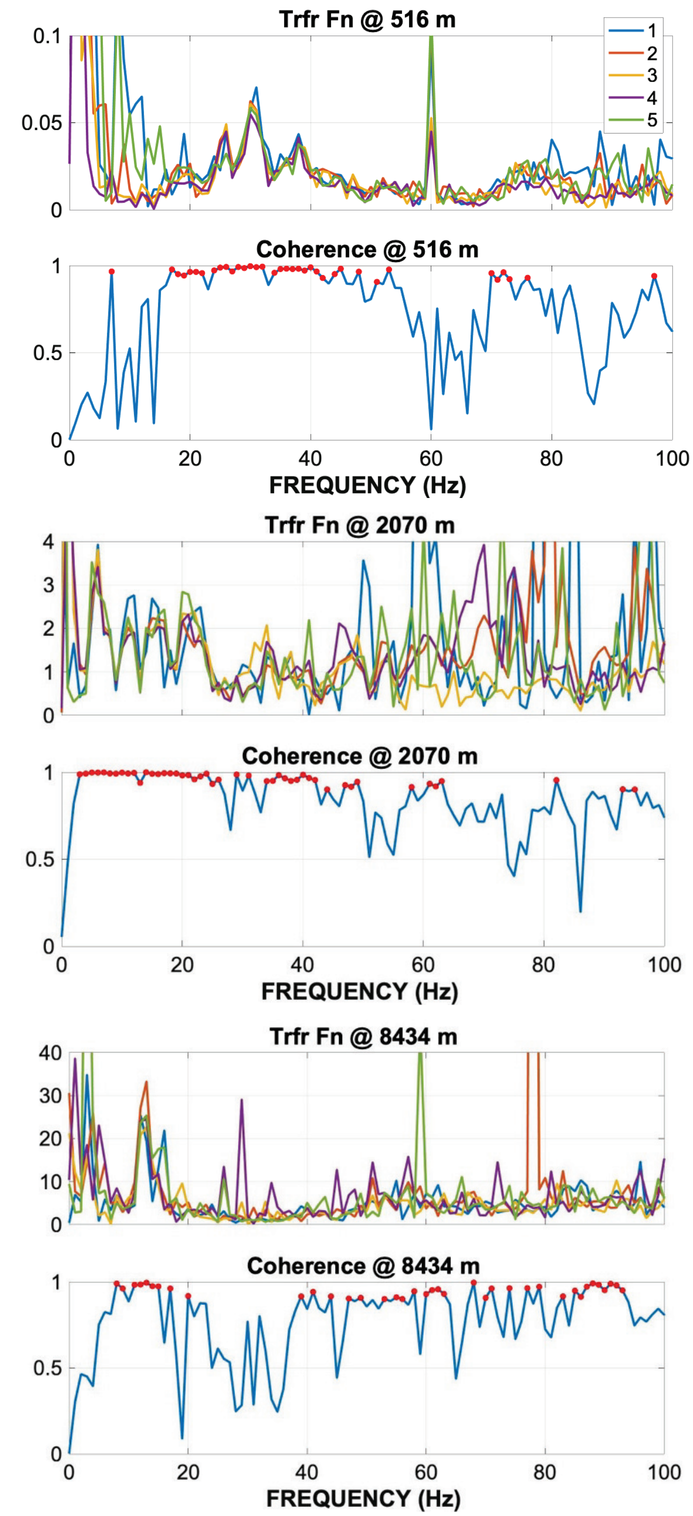

3.5.3 DOA estimation from seismometers

The are two ways to estimate the DOA, or back azimuth, from geophones. One method is to determine the time differences of arrival from an array of geophones. The second method is to process the signals from 3C geophones as vector sensors. Ideally, the particle motion determined from the horizontally oriented components should be parallel to the DOA. Both approaches were attempted here.

Two arrays of 3 vertical geophones were deployed at sites approximately 500 m and 2,000 m from the source. Unfortunately, only one of the sensors at the 2,000-m site functioned properly and recorded useful signals. The array at 500 m is shown in the middle plot in Figure 8. Only the two sensors to the north recorded useful signals in this array. A bearing was determined from the differences in the arrival times of the signals to each sensor using a procedure outlined by Mitchell (2012) and depicted in Figure 26. In the figure, the green dashed line segment of length *l* separates the two sensors, denoted by ‘x’ symbols; the green solid line is its perpendicular bisector. The solid blue line that intersects the green dashed line at the right sensor location represents the plane wavefront. The solid blue line with the arrow that is perpendicular to the wavefront represents the direction of travel of the wavefront. The wavefront reaches the sensor on the left a time Δt, later, which is the time difference between signals arriving at the two sensors. The wavefront travels a distance $d = \Delta t * c$ during this time, where c is the speed of sound. The angle θ between the wavefront and the perpendicular bisector is given by $sin^{-1}(d/l)$. The DOA, or back azimuth, is determined by adding this angle to the angle that the perpendicular bisector makes with true north, denoted β.

The signal recorded from the NW geophone from shot 3 is plotted in Figure 24. A similar signal was recorded with the NE geophone. The time difference between the two signals was determined as the difference between the times associated with the first negative peak; in this case, Δt = 0.049 sec, corresponding to a distance of $d = 16.560\ m$. This results in θ = 56.3° and a DOA of 58.1° (the angle between North and the perpendicular bisector is β = 1.87° in this case). The DOAs determined from the other shots varied from 56.4° to 60.0°.

For comparison, the bearing from the NW geophone to the source, as determine from GPS data, is 37.6°. Initially, it was thought that the error

Figure 26. Schematic showing geometry used to determine DOA. The green ‘x’ symbols represent the sensors. The blue line that intersects the sensor on the right represents a plane wave. The red dashed curve represents a spherical wave front originating from the source, exaggerated in drawing. Detailed explanation is provided in text.

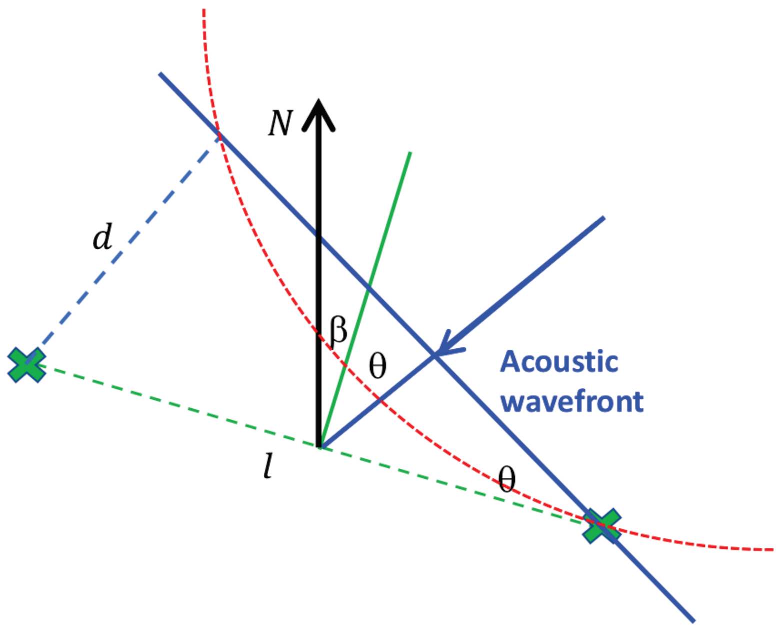

in the acoustically determined DOA arose because the sensors were too close to the source for the plane wave assumption to be valid. Radii from the source to the end points of the line segment represented by the two sensors span an arc of almost 2°. However, the error is too large to be caused by this assumption. To check this, the DOA was determined geometrically with GPS data using the same approach as in the acoustic case. The source-to-sensor distance for the NW and NE geophones were 518.20 and 506.83 m, respectively, the difference resulting in d = 11.37 m. Using the same formula in the paragraph above leads to θ = 34.82° and a DOA of 36.7°, which compares favorably with the direct GPS calculation. It was mentioned in Section 3.3 that the RT125A digitizers do not contain a GPS clock and that, although they had been synchronized prior to the test, they experienced drift. The amount of drift was determined after the test and corrections made for each digitizer. However, it seems that this was not sufficient to provide the accuracy needed for this type of measurement. The DOAs were recalculated without the time corrections. The averaged DOA in this case was 21.52°, which is an underestimate of the DOA.

The DOA was determined using this approach with the three microphone array at the Instrumentation site located near the 3C seismometers and shown in the bottom of Figure 8. Five DOAs were determined for each of the three pairs of microphones shown in the figure, N-S, W-S, and N-W. A sound speed of 345.0 m/s was used (Figure 16). The DOAs averaged over the five shots are 147.8°, 157.6°, and 149.4°, respectively. These values compare favorably with the 145.7° DOA determined geometrically. The DOA determined for all shots are listed in Table 8. It is believed that the estimates from the array could have been improved had the spacing between the sensors been larger, at least doubled. The sample rate used for these sensors was 500 Hz, and the largest separation between sensors was 3.54 m. The largest possible time difference between sensors (endfire condition) would be five samples (((3.535 m/345 m/s)*500 samples/s) = 5.1 samples), so the resolution would have been better had the sensor spacing or the sample frequency increased. (The undefined entry in the table results from the measured time difference giving a value of *d* larger than the sensor separation, which leads to taking the inverse *sine* of a number greater than 1, which may have been avoided with larger spacing.) Even though the sensor spacing nor sample rate were optimal, this example serves to validate the approach.

Table 8. Back azimuths measured with 3-microphone array shown in Figure 8 for all 5 shots. N-S, W-S, and N-W correspond to the 3 pairs of microphones at the vertices. The error is the difference between the measured azimuth and that determined from ground truth, 145.7°.

	N-S		W-S		N-W	
Shot	DOA	Error	DOA	Error	DOA	Error
1	159.4°	13.7°	Undefined	NA	147.2°	1.5 °
2	140.0°	-5.7°	157.6°	11.9°	147.2°	1.5 °
3	159.4°	13.7°	157.6°	11.9°	158.4°	12.7 °
4	140.0°	-5.7°	157.6°	11.9°	147.2°	1.5 °
5	140.0°	-5.7°	157.6°	11.9°	147.2°	1.5 °

DOA determined from treating 3C geophones as vector sensors met with a bit more success than with calculating the DOA from time differences measured with vertical geophones. As shown at the bottom of Figure 8, two 3-component geophones were placed at the Instrumentation site, one of which had a 1-Hz resonance frequency and the other 4.5 Hz. Both of these seismometers were oriented with the horizontal axes parallel to North-South and East-West directions. The horizontal components with respect to time are plotted in Figure 27. The hypothesis was that these sensors would behave like vector sensors and that the particle motion would be parallel to the DOA, or back azimuth, of the acoustic wave traveling from the source. However, the plots indicate that the directions of particle velocity are not consistent as the acoustic wave passes over the sensor.

Figure 27. The horizontal components plotted with respect to time for the 3C geophones located at 8,440 m and 8,434 m from the source.

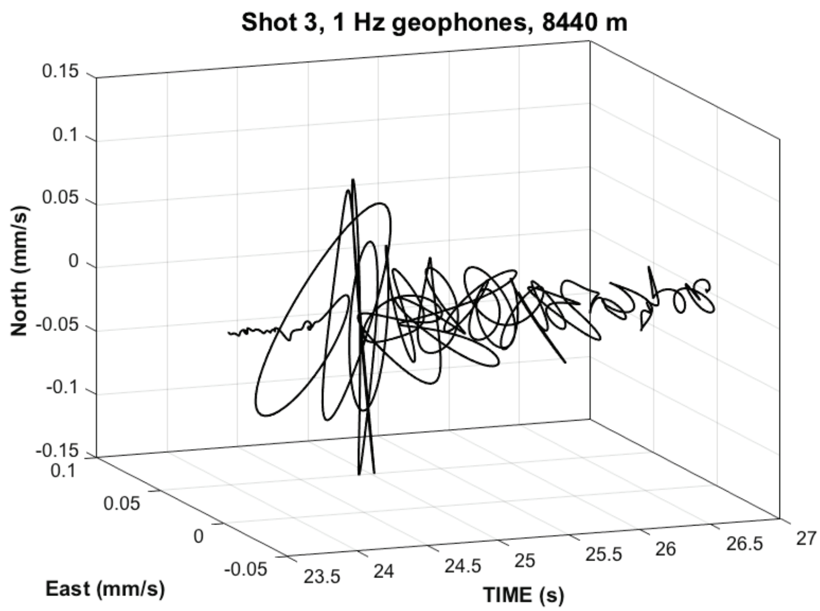

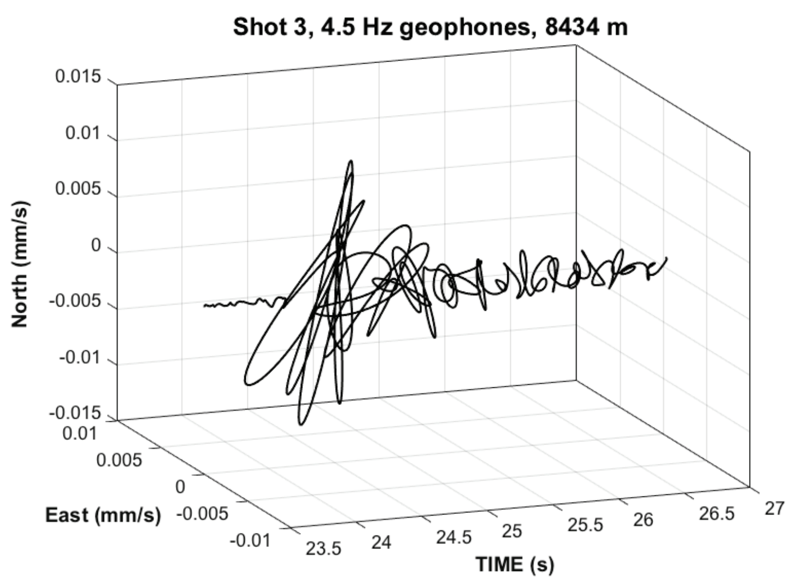

This is more obvious in the plots in Figure 28, in which the North-South and East-West components from shot 3 and for both 3C seismometers are plotted against each other. The signals were bandpass filtered from 1 to 20 Hz. The period of the first cycle of the signal recorded with the microphone at 8,434 m (Figure 24) was 0.07 sec, which corresponds to a frequency of 14.3 Hz. The periods of the first couple of cycles of the N-S oriented 1-Hz seismometer varied from 0.076 to 0.09 sec, corresponding to frequencies in the 11 to 13 Hz range. The periods and frequencies associated with the 4.5-Hz seismometers were similar. The cutoff frequencies for the bandpass filter were selected to extend from the resonance frequency of the seismometer to include the fundamental period of oscillation. The geophones are most sensitive and accurate at the flat part of their response curve, above 1 Hz and 4.5 Hz, respectively.

Figure 28. The horizontal components plotted for different time segments for the 3C geophones located at 8,440 m (top) and 8,434 m (bottom) from the source. In each plot, the black line is parallel to the back azimuth from the receiver to the source, calculated from GPS data.

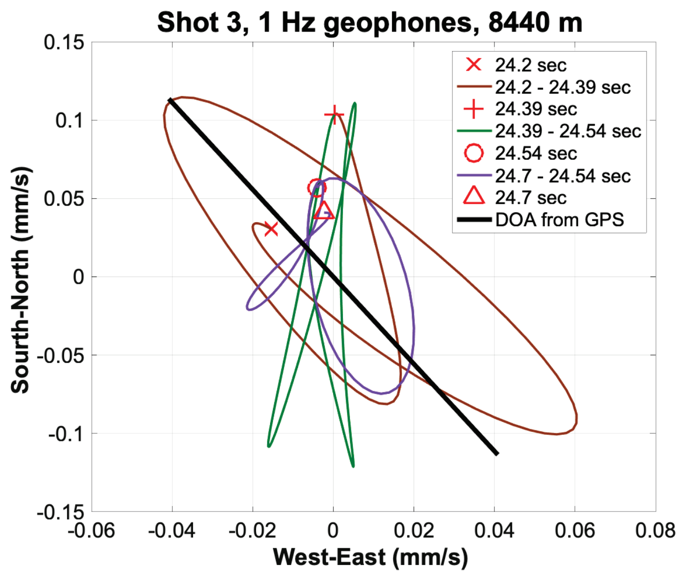

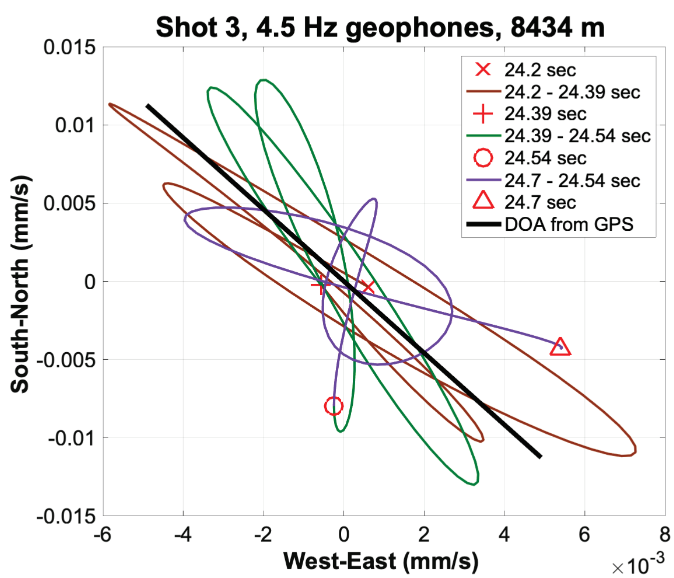

The Lissajous curves shown in Figure 28 were divided into three different time segments and color coded in order to track the progression of the oscillations with time. The first couple of oscillations, plotted in brown, have larger amplitudes and represent the arrival of the signal. These oscillations run from the NW to SE direction. Subsequent cycles have smaller amplitudes, and their directions are less consistent and defined. Similar curves for all five shots recorded with both 3C seismometers are included in Appendix E.

The angle associated with the first (brown) cycle was calculated by finding the points in the extreme NW and SE ends of the loop. These points define a line segment that runs in the NW to SE direction. The ratio of the NS to EW components determine the slope of the segment, and the inverse tangent of this ratio determines the angle from the West direction. The angles for the first cycle were determined to be 64.0° and 59.6° for the 1 Hz and 4.5 Hz geophones, respectively, corresponding to back azimuths of 154.0° and 149.6°. The back azimuth from the sensor location to the source, determined from the GPS data, was calculated to be 145.7°. This is a difference of 8.3° for the 1 Hz sensor and 3.9° for the 4.5 Hz sensor.

The back azimuth was calculated from the Lissajous curves of the first cycles for all five shots, and the results are listed in Table 9. The azimuths determined from the curves are consistent for each sensor; however, the errors corresponding to the 4.5-Hz sensor appear to be smaller. The larger error in the 1-Hz sensors could be due to errors in sensor alignment or to the heterogeneity of the soil. The fact that the errors associated with the 1-Hz seismometer are all positive supports the argument that the error was due to alignment. Another possible source of error may be generated by the physical construction of the seismometers used in this study. Unlike true three-component borehole or pier-mounted seismometers used for earthquake measurements, the rapid-installation, fully contained geophones do not have decoupled components. The components are located in the same fixture, rather than separately as would be done for an isolated estimation of DOA. Azimuthal resolution may also be different in the 1-Hz and 4.5-Hz geophones due to sensitivity and frequency component of the signal.

Only the first cycle, which has the largest amplitude, produces a measured DOA close to the true back azimuth. The changes in particle velocity direction after the first couple of cycles could be due to reflection of the leading wavefront off of nearby structures or diffraction effects caused by trees and shrubs. The seismometers were located in a residential neighborhood with houses spaced roughly 50 to 100 m apart. Subsequent cycles appear to rotate in the clockwise direction, which could be caused by such a reflection. Qualitatively, the orientation of the subsequent cycles is somewhat consistent for a given seismometer, but different between seismometers, which would be consistent with multi-path issues. This could be worth investigating more quantitatively, but this would require a more controlled experiment and is outside the scope of this report.

Table 9. Back azimuths measured with 3C seismometer and geophone for all 5 shots. The error is the difference between the measured azimuth and that determined from ground truth, 145.7°.

	1 Hz Seismomter		4.5 Hz Seismometer	
Shot	DOA	Error	DOA	Error
1	157.9°	12.2°	151.6°	-5.9°
2	153.8°	8.1°	138.3°	-7.4 °
3	154.0°	8.3°	149.6°	3.9°
4	159.4°	13.7°	146.6°	0.9°
5	147.8°	2.1°	149.3°	3.6°

As these are air-coupled waves, some error in the azimuth could be due to meteorological changes along the path due to the time-evolving acoustic medium. If the analysis is only of the first arrival, and these are air-coupled seismic recordings, not direct seismic waves, then the azimuthal error variance could be a reflection of the atmospheric turbulence during the propagation path, i.e., the inconsistency of back azimuths between shots on the same sensor would suggest atmospheric path effects manifesting as azimuthal anomalies. For instance, the maximum error from the three elements of the microphone array correspond to shot 3 (Table 8) suggesting an atmospheric path effect. However, the errors obtained with the 3C seismometers are not consistent with this observation. This atmospheric variability is not captured by the meteorological measurements obtained in this study, as only pre-and post-shot radiosonde profiles were collected. Future investigations of meteorological complexities are planned, with model validation of experimental meteorological measurements.

Back azimuth errors range from 2.1° to 12.2° for the 1-Hz seismometer (total 10.1 deg) and -7.4° to 3.9° for the 4.5-Hz seismometer (total 11.3°). This range of variance from the true azimuth is comparable to that obtained with the microphone array. The maximum variance from the microphone array was 19.4°; however, a significant source of error was due to discretization effects.

4 Summary

A number of different sensors, high-frequency pressure gauges, infrasound sensors, broadband microphones, and seismometers were deployed at different ranges to record acoustic and seismic signals produced by explosive sources. Five spherical charges, with different weights, were detonated to create the acoustic events needed to study acoustic and seismic propagation over ranges from 3 m to 13 km. Some of the signals were clipped because their amplitudes exceeded dynamic range of some of the sensors, especially for the larger charges and closer ranges. In spite of this, the experiment provided useful data that can be used for propagation modeling and other purposes.

A model represented by Equation 2 was applied to the data in which the peak amplitude was plotted versus scaled distance with reasonably good agreement. Discrepancies at the longer ranges were associated with the use of porous hose wind filters.

Furthermore, measurements of the time of arrival (TOA) of the different signals were collected and plotted. Changes in the wave speed were observed as the wave propagated from the strongly non-linear regime in the near-field, to weakly non-linear regime in the mid-field range, to linear in the far-field range. In the near-field range, the behavior is highly non-linear, especially when observing the TOA from shot 4 (24-lb charge), which created the largest acoustic pressure amplitudes. Here, shock-wave speeds up to 702 m/s at ranges close to the source were observed. The shock speeds associated with shot 1 were lower due to its smaller pressure amplitudes, although still non-linear. On the other hand, the signals from all shots were linear in the far-field range.

The acoustic signals were recorded at a site 8.4 km from the detonation in which sensors were deployed with different types of wind filters. While no approach could be identified clearly superior to the others, some were definitely inferior. As an example, a Chaparral was buried in leaves. Although the background noise recorded with this sensor was very low, so was the signal, which suggested that the leaves actually smothered the sensor. The Chaparral with coiled hoses did not perform well either. The Hyperion under the papasan was not very sensitive to low frequencies, below 20 Hz, which was surprising. But it is believed that this sensor was defective.

Seismometers were also deployed to detect and measure the disturbances produced by the blast. Geophones deployed within 125 m from the blast were able to detect the resulting seismic waves. Seismometers at distances of over 8 km were able to detect the airborne shock waves. The times of arrivals determined and acoustic velocity measured with the geophones compared favorably with measurements made with infrasound sensors. In addition, comparison of waveforms with nearby geophones demonstrated the fidelity with which the geophones recorded the acoustically coupled seismic signals.

Finally, measurements with geophones were used to determine the DOA of the acoustic wave produced by the explosions. The method of using time differences of arrival between elements of an array of geophones was unsuccessful because of clock drift in the digitizers used. In a different approach, 3C seismometers were used to determine DOA of the airborne shock wave at distances of over 8 km. The horizontal components were processed to determine the particle motion, which was assumed to be parallel with the DOA. The results of this approach were effective. Although the results were consistent for each sensor, they were accompanied with some error. Also, the results were good only for the initial arrival of the wave. Pressure fluctuations from the tail of the wave form produced ambiguous results.

In all, the Multi-Objective Source Scaling Experiment achieved most of the objectives for which it was named. It studied and analyzed the TOA of signals, the effectiveness of different designs of wind filters, the coupling between acoustic and seismic signals, and the DOA estimation of the acoustic and seismic signals. This effort may be used as a reference for future experiments and as a source of data for comparison to modelling efforts.

References

Albert, D. G., S. Taherzadeh, K. Attenborough, P. Boulanger, and S. N. Decato. 2013. Ground vibrations produced by surface and near-surface explosions. *Applied Acoustics* 74:1279-1296.

Embleton, T. F. 1996. Tutorial on sound propagation outdoors. *The Journal of the Acoustical Society of America* 100:31-48.

Engineer Research and Development Center (ERDC). 2001. *Geotechnical and Structures Laboratory BlastX v.4.2 computer file*. Vicksburg, MS: U.S. Army Engineer Research and Development Center.

Haak, H. W., and G. J. De Wilde. 1996. Microbarograph systems for the infrasonic detection of nuclear explosions. Royal Netherlands Meteorological Institute, Seismology Division, WR 96-06.

Howard, W., K. Dillion, and F. D. Shields. 2007. Acoustical properties of porous hose wind noise filters. *Journal of the Acoustical Society of America* 122:2985 doi: 10.1121/1.2942646.

Kim, T. S., C. Hayward, and B. Stump. 2004. Local infrasound signals from the Tokachi-Oki earthquake. *Geophysical Research Letters* 31(20).

Kingery, C., and G. Bulmash. 1984. *Airblast parameters from TNT spherical air burst and hemispherical surface burst*. ARBR:-TR-02555. Aberdeen Proving Ground, MD: U.S. Army Armament Research and Development Center, Ballistic Research Laboratory.

Kinney, G. F., and K. J. Graham. 1985. *Explosive shocks in air* (2nd edition). New York: Springer.

Mitchell, A. J. 2012. *Technology for artillery location, 1914-1970*. Glasgow: Lulu.com.

Noel, S. D., and R. W. Whitaker. 1991. *Comparison of noise reduction systems*. Los Alamos National Laboratory Technical Report LA-12003-MS. Los Alamos, NM: LANL.

Pater, L. 1981. *Far field overpressure from TNT explosions: A survey of available models*. NSWC TR 81-132. Dahlgren, VA: Naval Surface Warfare Center.

Pierce, A. D. 1989. The wave theory of sound. In *Acoustics: An introduction to its physical principles and applications,* 29. New York: McGraw-Hill.

Shin, K., and Hammond, J. K. 2008. *Fundamentals of signal processing for sound and vibration engineers*. Chichester: John Wiley & Sons.

Swearingen, M. E., M. J. White, S. A. Ketcham, and M. H. McKenna. 2013. Use of a porous material description of forests in infrasonic propagation algorithms. *JournAlal of Acoustical Society of America* 2647-2659.

Walker, K., and M. Hedlin. 2010. A review of wind-noise reduction methodologies. In *Infrasound monitoring for atmospheric studies*. New York: Springer.

Whitaker, R. W., and D. E. Norris. 2008. Infrasound propagation. In *Handbook of signal processing in acoustics,* ed. R. W. Whitaker, D.E. Norris, D. Havelock, S. Kuwano, and M. Vorlander, 1497-1519. New York: Springer New York.

Appendix A: Photograph of the Sensors Deployed at Instrumentation Site

Appendix B: Time Series Recorded at Instrumentation Site

Time series recorded with Chaparral sensors at Instrumentation site from all five shots, as shown in Figure 18. For sensor numbers see Table 6.

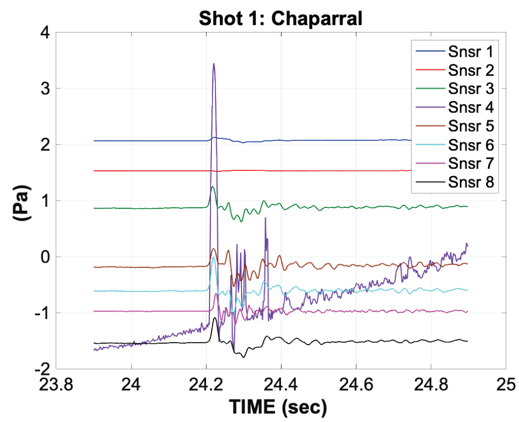

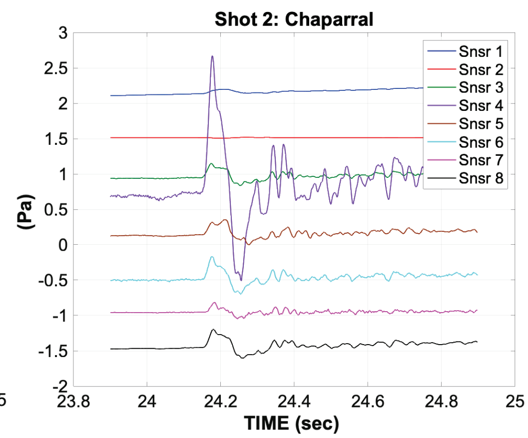

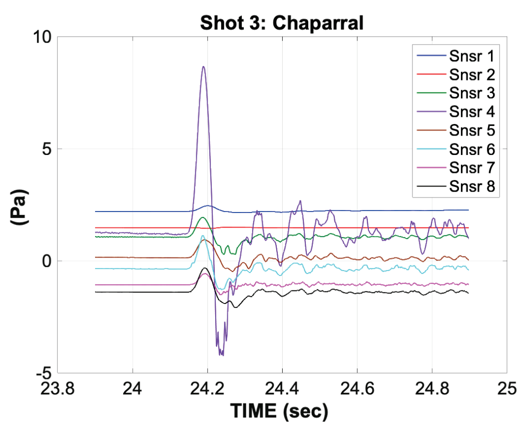

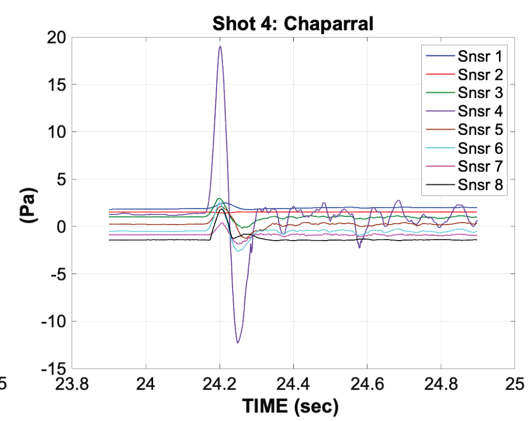

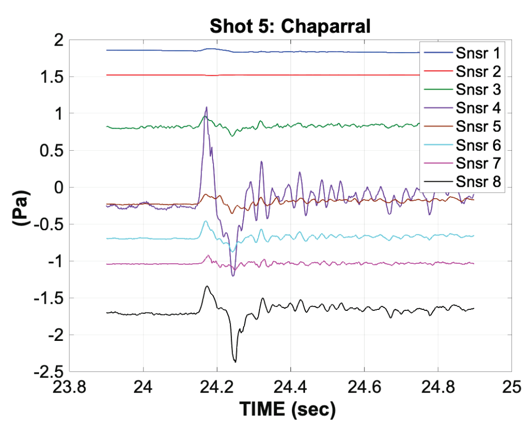

Time series recorded with IML and Hyperion sensors at Instrumentation site from all five shots, as shown in Figure 18. For sensor numbers see Table 6.

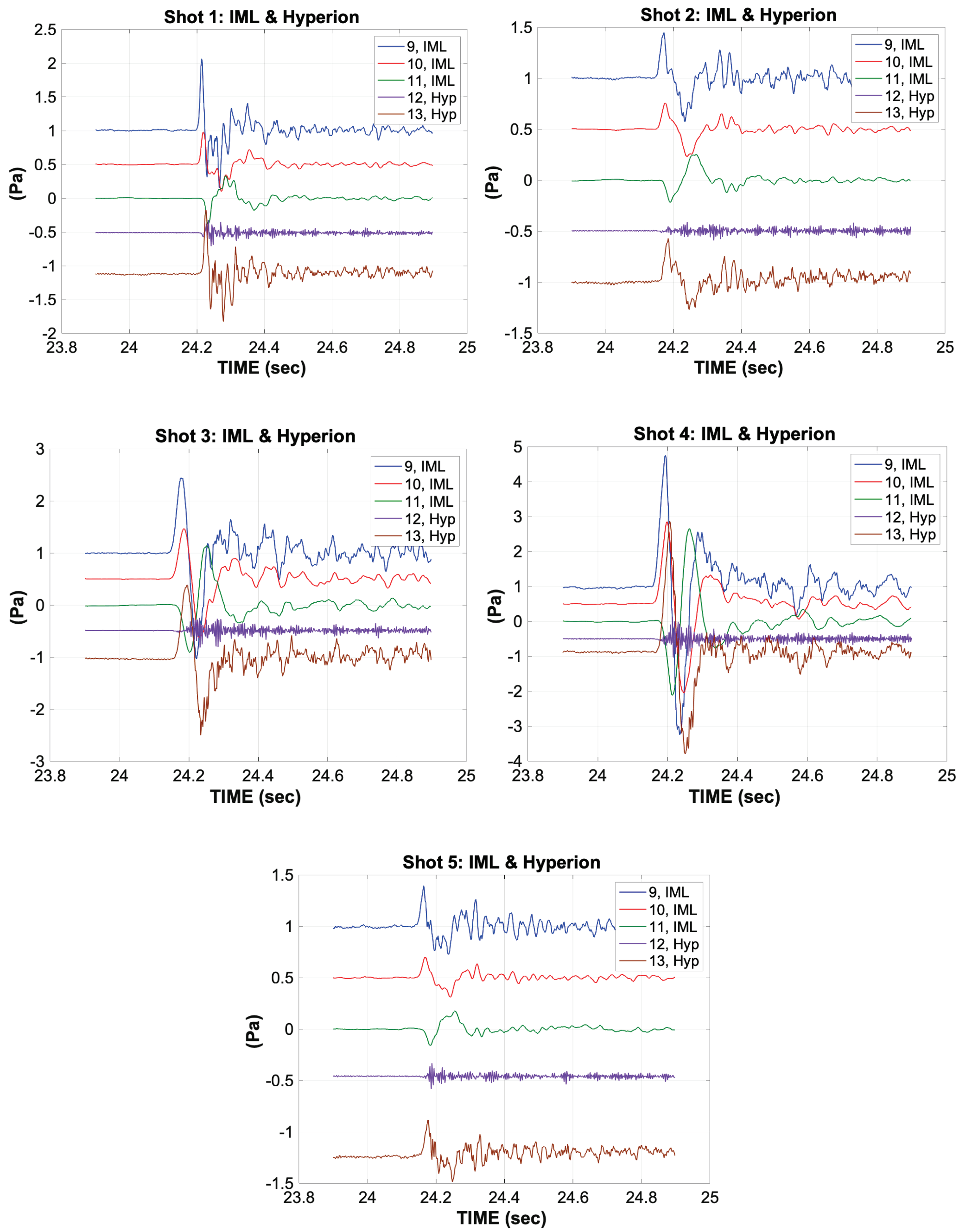

Appendix C: Background Noise Recorded at Instrumentation Site

Background noise recorded with Chaparral sensors at Instrumentation site from all five shots and used to determine SNR, as shown in Figure 19. For sensor numbers see Table 6.

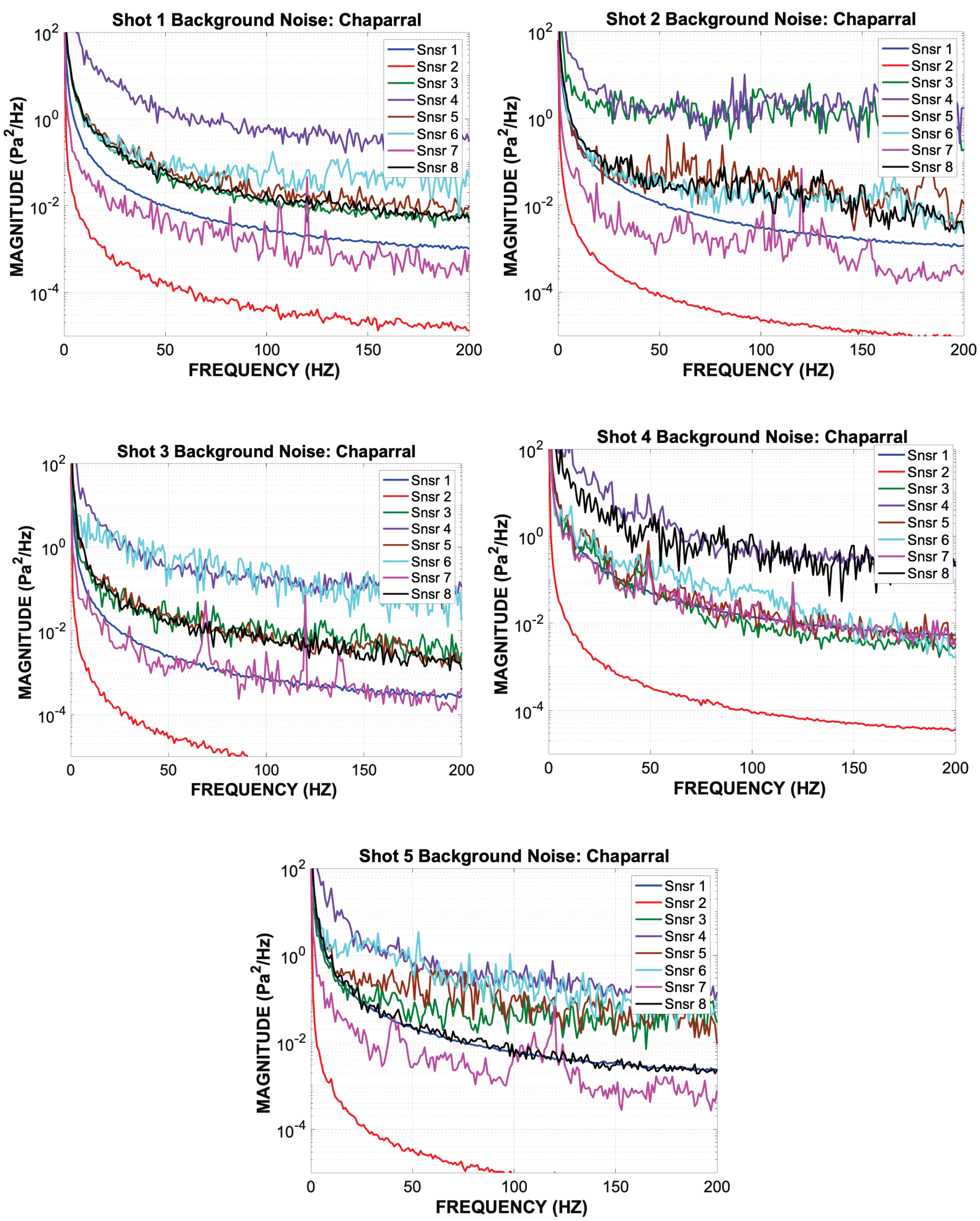

Background noise recorded IML and Hyperion sensors at Instrumentation site from all five shots and used to determine SNR. For sensor numbers see Table 6.

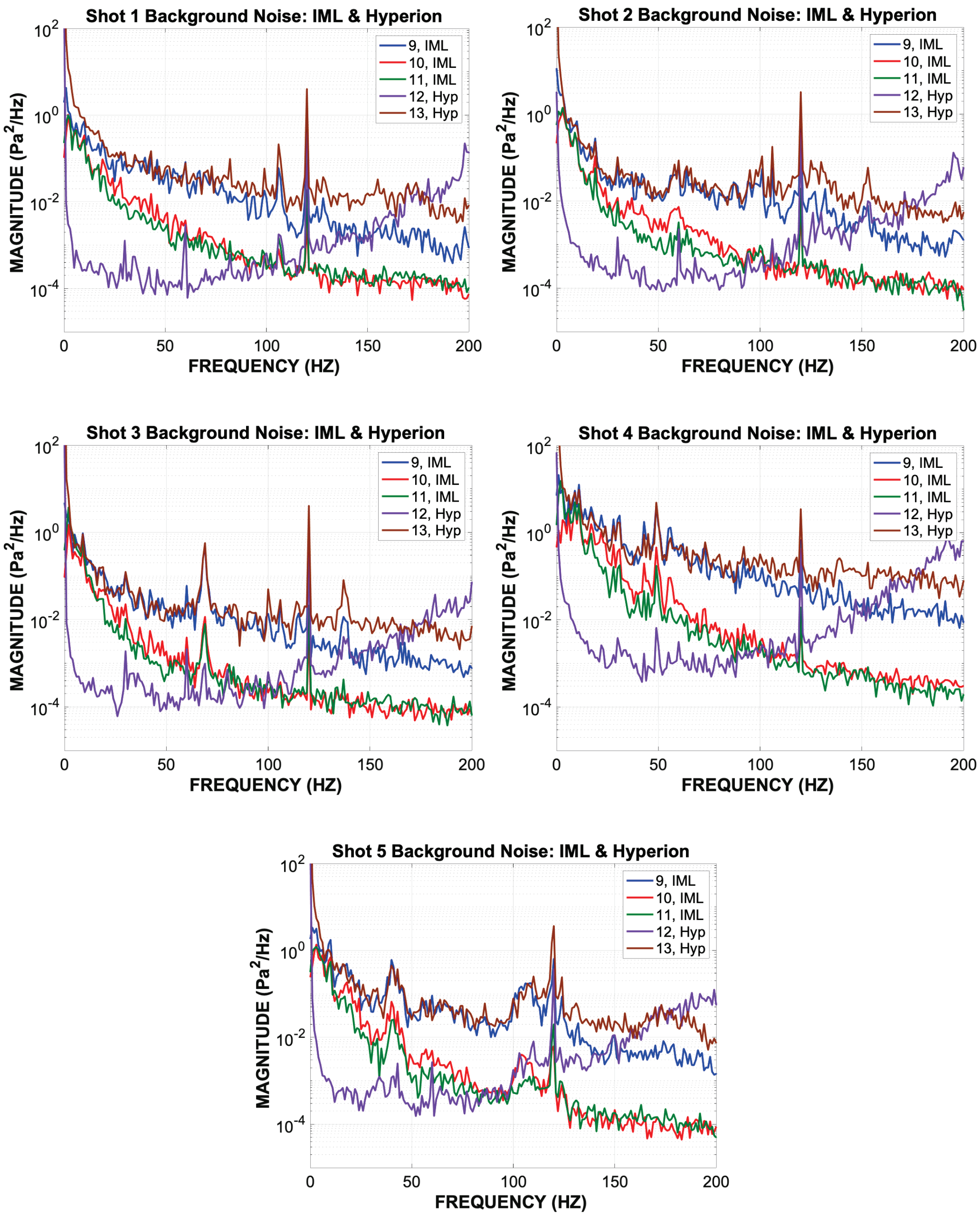

Appendix D: SNR Recorded at Instrumentation Site

SNR associated with Chaparral sensors at Instrumentation site from all five shots as shown in Figure 20. For sensor numbers see Table 6.

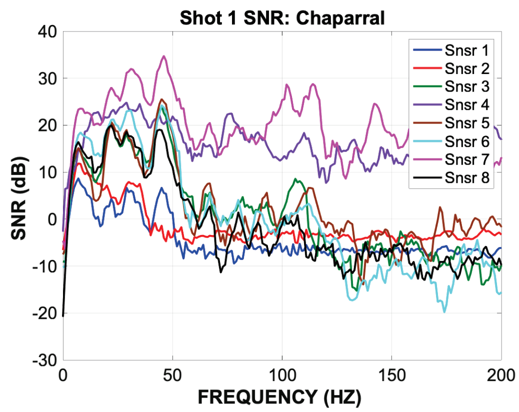

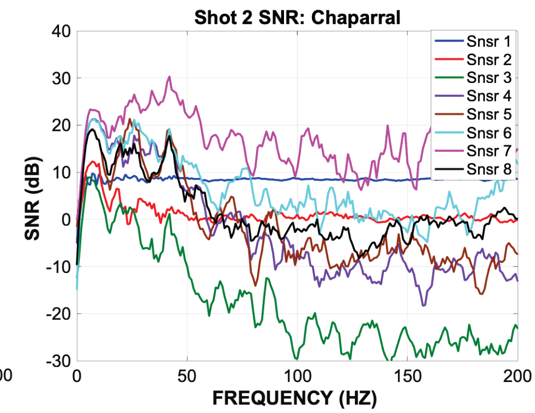

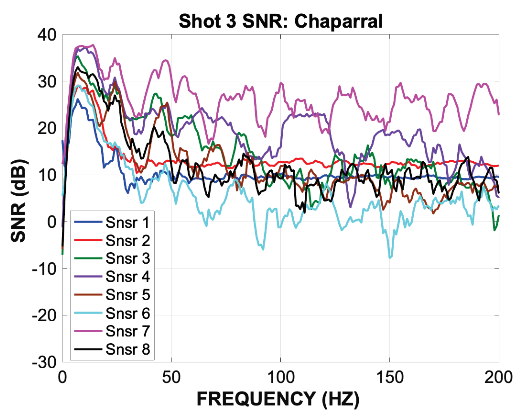

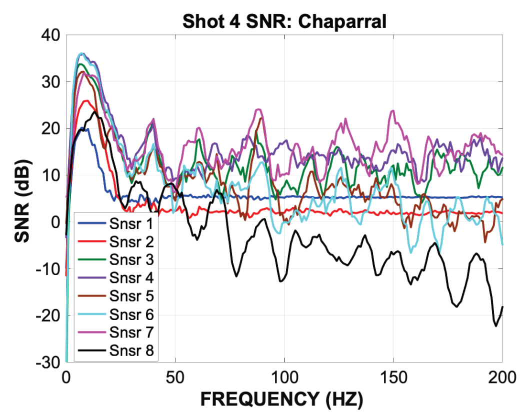

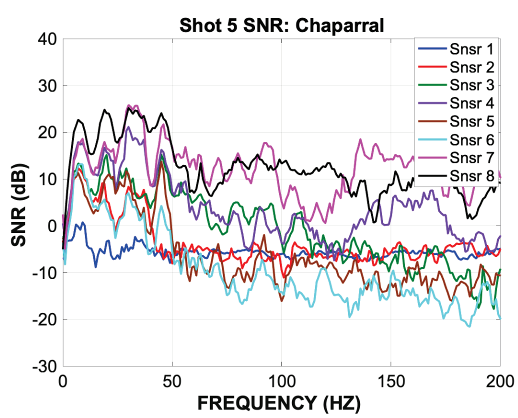

SNR associated with IML and Hyperion sensors at Instrumentation site from all five shots. For sensor numbers see Table 6.

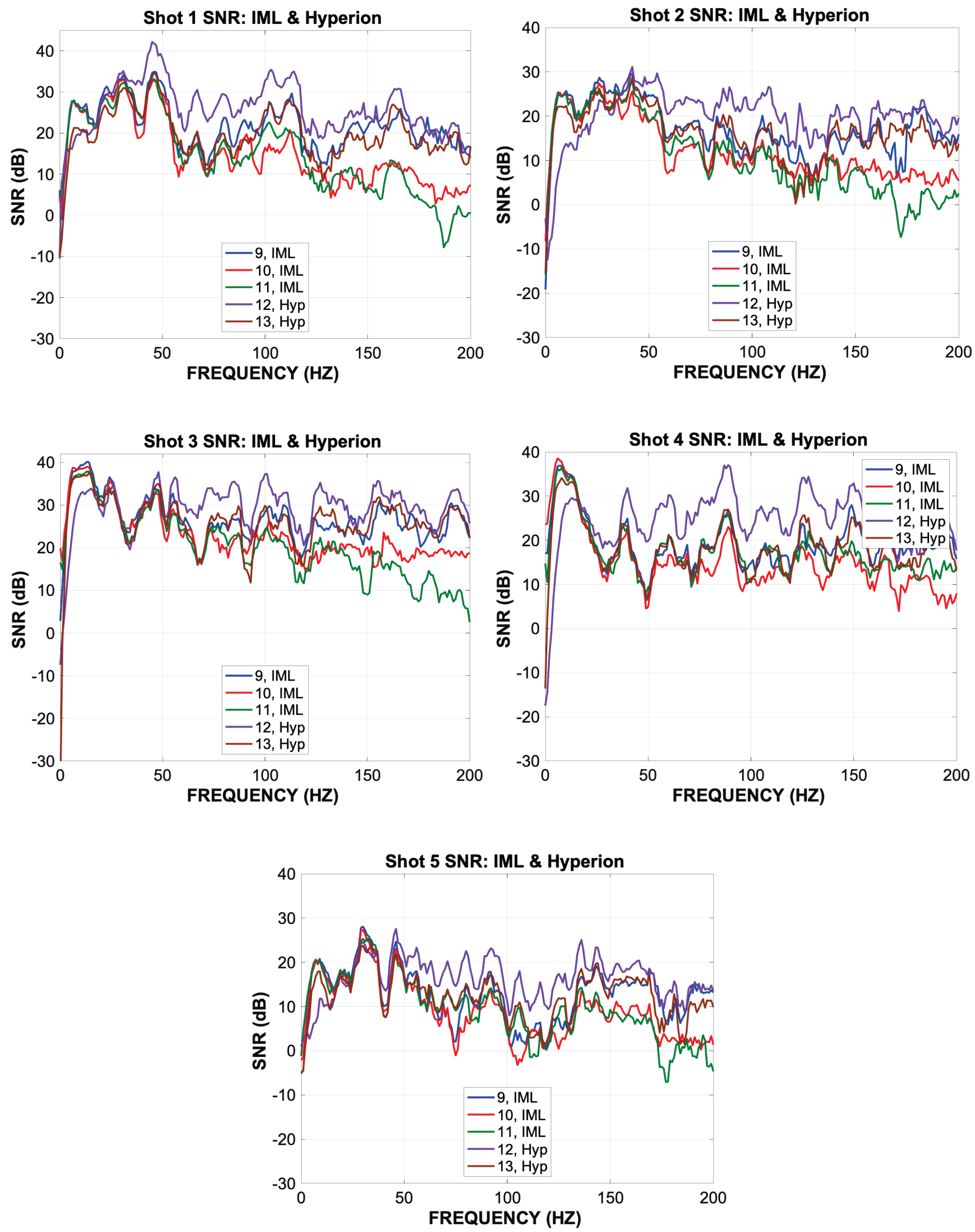

Appendix E: Seismometer Response to Acoustic Waves Produced by Airblast

The horizontal components plotted for different time segments for the 3C geophones located at the Instrumentation site, as shown in Figure 28.

1 Hz geophones located 8440 m from the source:

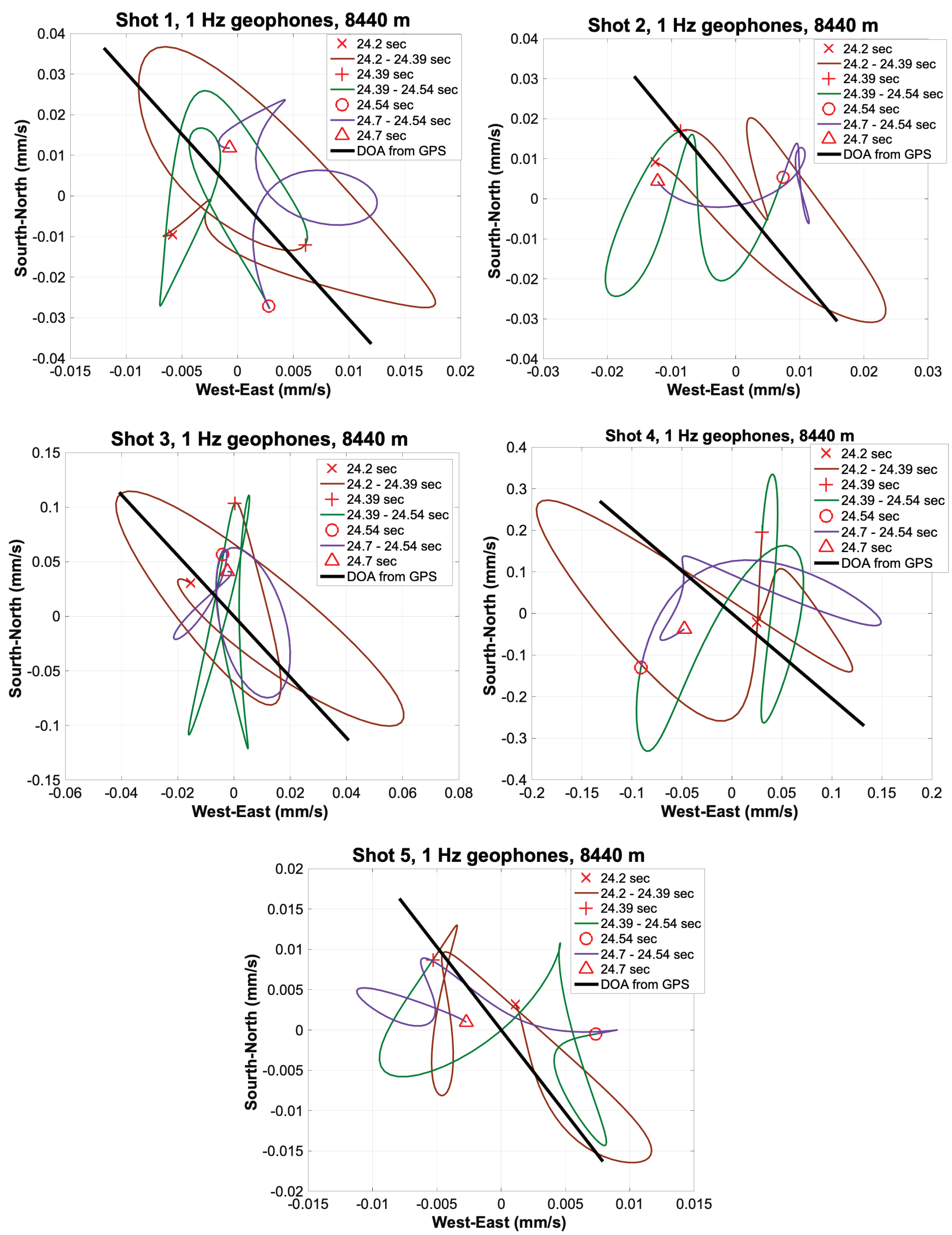

4.5 Hz geophones located 8434 m (bottom) from the source:

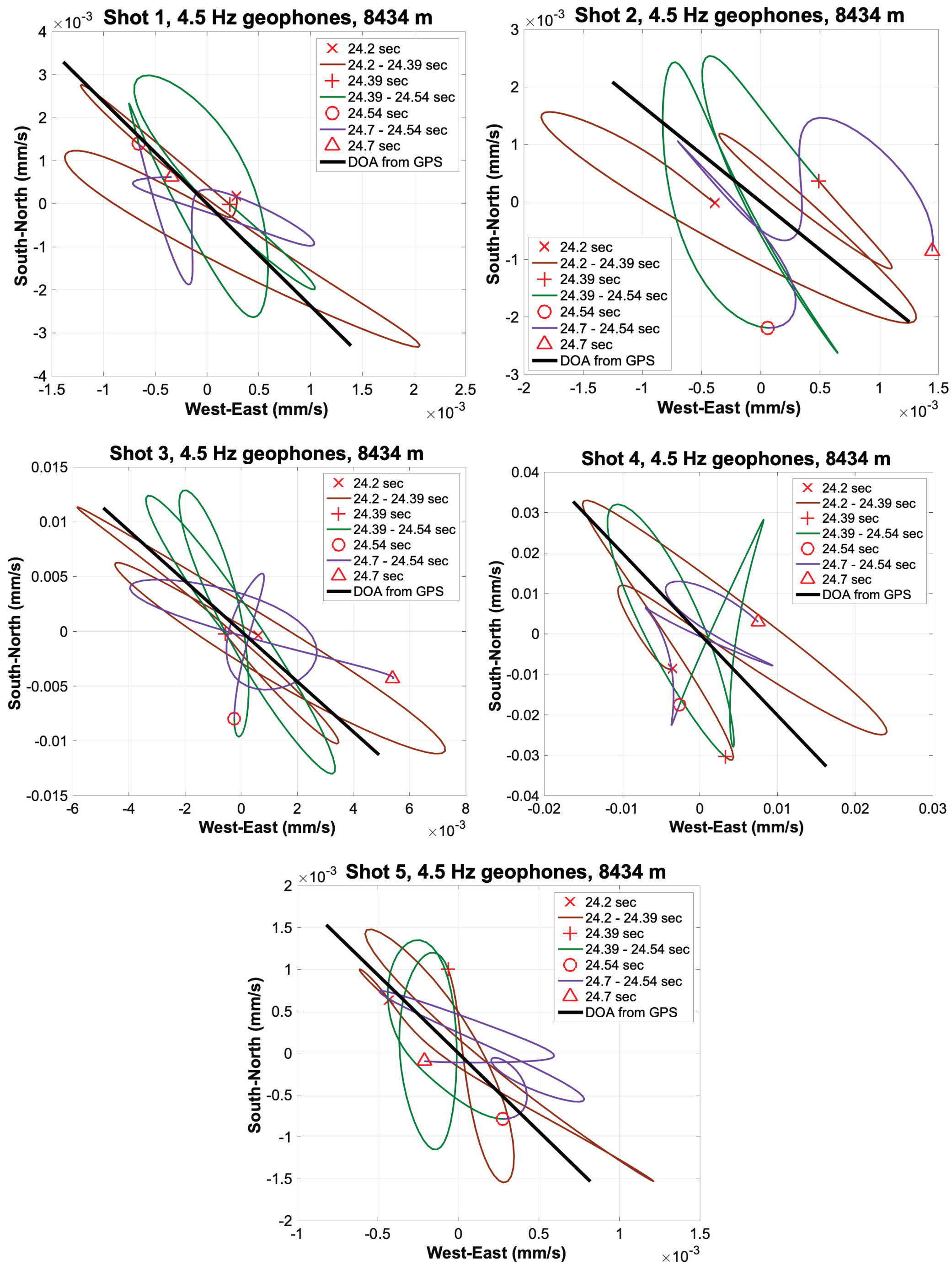

Unit Conversion Factors

Multiply	By	To Obtain
Pounds (Mass)	0.454	Kilograms
Pounds (Force)	4.45	Newtons
Pounds (Force) per square inch	0.006895	MegaPascals
Feet	0.3048	Meters
Miles	1.61	Kilometers

REPORT DOCUMENTATION PAGE

Form Approved OMB No. 0704-0188

1. REPORT DATE *(DD-MM-YYYY)* June 2021	**2. REPORT TYPE** Final	**3. DATES COVERED** *(From - To)*

4. TITLE AND SUBTITLE
Multi-Objective Source Scaling Experiment

5a. CONTRACT NUMBER

5b. GRANT NUMBER

5c. PROGRAM ELEMENT NUMBER
622146

6. AUTHOR(S)
R. Daniel Costley, Luis A. De Jesús Díaz, Sarah McComas, Christopher P. Simpson, James W. Johnson, and Mihan H. McKenna

5d. PROJECT NUMBER
AR9

5e. TASK NUMBER
02

5f. WORK UNIT NUMBER

7. PERFORMING ORGANIZATION NAME(S) AND ADDRESS(ES)

Geotechnical and Structures Laboratory
U.S. Army Engineer Research and Development Center
3909 Halls Ferry Road
Vicksburg, MS 39180-6199

Information Technology Laboratory
U.S. Army Engineer Research and Development Center
3909 Halls Ferry Road
Vicksburg, MS 39180

8. PERFORMING ORGANIZATION REPORT NUMBER
ERDC TR-21-10

9. SPONSORING / MONITORING AGENCY NAME(S) AND ADDRESS(ES)
U.S. Army Corps of Engineers
Washington, DC 20314-1000

10. SPONSOR/MONITOR'S ACRONYM(S)

11. SPONSOR/MONITOR'S REPORT NUMBER(S)

12. DISTRIBUTION / AVAILABILITY STATEMENT
Approved for public release; distribution is unlimited.

13. SUPPLEMENTARY NOTES

Conducted for the Office of the Assistant Secretary of the Army for Acquisition, Logistics, and Technology (ASAALT) under Project 62784/T40/24, "Remote Assessment of Critical Infrastructure" (RACI), and task 622146/AR9/02, "Remote Assessment of Infrastructure for Ensured Maneuver" (RAFTER) under the Persistent Geophysical Sensing – Infrasound (PGSI)

14. ABSTRACT

The U.S. Army Engineer Research and Development Center (ERDC) performed an experiment at a site near Vicksburg, MS, during May 2014. Explosive charges were detonated, and the shock and acoustic waves were detected with pressure and infrasound sensors stationed at various distances from the source, i.e., from 3 m to 14.5 km. One objective of the experiment was to investigate the evolution of the shock wave produced by the explosion to the acoustic wavefront detected several kilometers from the detonation site. Another objective was to compare the effectiveness of different wind filter strategies. Toward this end, several sensors were deployed near each other, approximately 8 km from the site of the explosion. These sensors used different types of wind filters, including the different lengths of porous hoses, a bag of rocks, a foam pillow, and no filter. In addition, seismic and acoustic waves produced by the explosions were recorded with seismometers located at various distances from the source. The suitability of these sensors for measuring low-frequency acoustic waves was investigated.

15. SUBJECT TERMS

Infrasound	Acoustic-to-sesmic coupling	Airblast
Outdoor sound propagation	Near-surface explosion	Explosives
Sound-Detectors	Wind-noise	Shock waves
	Winds	Sound-waves

16. SECURITY CLASSIFICATION OF:			**17. LIMITATION OF ABSTRACT**	**18. NUMBER OF PAGES**	**19a. NAME OF RESPONSIBLE PERSON**
a. REPORT	**b. ABSTRACT**	**c. THIS PAGE**			**19b. TELEPHONE NUMBER** *(include area code)*
Unclassified	Unclassified	Unclassified	SAR	71	